

**EXPERIMENTAL STUDY OF AEROSOL
DEPOSITION IN DISTAL LUNG BRONCHIOLES**

A THESIS

submitted by

ARNAB KUMAR MALLIK

for the award of the degree

of

MASTER OF SCIENCE

(by Research)



**DEPARTMENT OF APPLIED MECHANICS
INDIAN INSTITUTE OF TECHNOLOGY MADRAS.**

AUGUST 2020

THESIS CERTIFICATE

This is to certify that the thesis titled **EXPERIMENTAL STUDY OF AEROSOL DEPOSITION IN DISTAL LUNG BRONCHIOLES**, submitted by **ARNAB KUMAR MALLIK (AM17S032)**, to the Indian Institute of Technology, Madras, for the award of the degree of **Master of Science**, is a bona fide record of the research work done by him under my supervision. The contents of this thesis, in full or in parts, have not been submitted to any other Institute or University for the award of any degree or diploma.

Mahesh V. Panchagnula
Research Guide
Professor
Dept. of Applied Mechanics
IIT Madras, 600 036

Place: Chennai

Date:

*Dedicated to my parents, wife
& family...*

ACKNOWLEDGEMENTS

I am highly indebted to *Prof. A.K. Mishra* from Department of Chemistry and *Prof. Anju Chadha* from Department of Biotechnology, IIT Madras for providing their lab facilities for some of the experiments.

I acknowledge *Defense Research and Development Organization (DRDO)* for supporting me financially to earn my MS degree from IIT Madras.

I thank my General Test Committee members, *Dr. Satyanarayanan Seshadri* and *Dr. Manikandan Mathur* for their support.

I thank the *Head*, Department of Applied Mechanics, IIT Madras for maintaining a healthy research environment in our department. I also acknowledge various helps of *lab assistants* and *other staffs* of our department.

I gratefully acknowledge my lab mates for their constant support and selfless co-operation throughout my MS degree program.

Finally, I gratefully acknowledge my advisor, *Prof. Mahesh V. Panchagnula*, who not only guided me for my thesis but also enlightened me with other dimensions of life that made me a better human. I pay my humble gratitude and deepest sense of respect to him.

ABSTRACT

KEYWORDS: Aerosol, distal lungs, Reynolds number, deposition model.

The deposition of micron particles finds importance in meteorology and several engineering applications such as deposition of dust in gas lines, carbon deposition in engine exhaust, designing effective air-cleaning systems and estimating deposition of inhaled drug or atmospheric pollutants to determine its consequences on human health. Although the existing literature on deposition in straight tubes is quite mature, an experimental study on deposition in micro capillaries with a wide ranges of Re that models particle dynamics in lungs, is missing. The deposition of atmospheric pollutants and nebulized drugs in the lung depends on various biological factors such as flow properties, lung morphology, breathing patterns, particle properties, deposition mechanism, etc. To complicate matters, each breath manifests flows spanning a wide range of Reynolds numbers ($10^{-2} \leq Re \leq 10^3$) in various regions of the lung.

In this study, the deposition of nebulized aerosol was experimentally investigated in phantom bronchioles of diameters relevant to the 7th to the 23rd branching generations and over the entire range of Re manifest during one breathing cycle. The aerosol fluid was loaded with boron doped carbon quantum dots as a fluorophore. An aerosol was generated of this mixture fluid using an ultrasonic nebulizer, producing droplets of $6.5\mu m$ as the mean diameter. The amount of aerosol deposited on the bronchiole walls was measured using a spectrofluorometer. The experimental results show that dimensionless deposition (δ) varies inversely with the bronchiole aspect ratio (\bar{L}), with the effect of Reynolds number (Re) being significant only at low \bar{L} . δ also increased with increasing dimensionless bronchiole diameter (\bar{D}). However, it is invariant with the particle size based Reynolds number. It was observed that deposition can be distinguished into three distinct regimes based on Re - impaction dominated deposition (for $10 \leq Re \leq 10^3$), sedimentation dominated deposition (for $1 < Re < 10$) and diffusion dominated deposition (for $10^{-2} \leq Re \leq 1$). We also show that $\delta\bar{L} \sim Re^{-2}$ for $10^{-2} \leq Re \leq 1$, which is typical of diffusion dominated regime. For $Re > 1$,

$\delta\bar{L}$ is independent of Re , which is typical of impaction dominated regime. We also show a crossover regime where sedimentation becomes important. Finally, a universal bronchiole scale deposition model is proposed which can form the building block for lung-scale aerosol deposition prediction.

The effect of breathing frequency and breath hold time on regional lung deposition is estimated from the experimentally developed model. Lower breathing frequency and higher breath hold time magnifies the deposition in the alveolar region which is highly desirable for efficient drug delivery. But for atmospheric pollutants and virus laden droplets, the low breathing rate accompanied with high breath hold time can highly affect human health.

TABLE OF CONTENTS

ACKNOWLEDGEMENTS	ii
ABSTRACT	iii
LIST OF TABLES	vii
LIST OF FIGURES	xi
ABBREVIATIONS	xii
NOTATION	xiii
1 INTRODUCTION	1
1.1 Lung Morphology	1
1.2 Breathing Mechanism	3
1.3 Transport of Aerosol Particles in Lungs	4
1.4 Motivation	6
1.5 Objectives	8
1.6 Overview of the thesis	9
2 Literature Survey	11
2.1 Determination of lung morphometry	11
2.2 Deposition studies on throat model	13
2.3 Deposition studies in the upper lung	14
2.4 Deposition study in deep lung model	15
3 Experimental Methods	18
3.1 Experimental setup	18
3.2 Preparation of aerosol liquid	20
3.3 Generation and characterization of aerosol plume	22
3.4 Preparation and analysis of deposition samples	27

4	Results and Discussion	28
4.1	Experimental Parameters	28
4.2	Effect of \bar{L} , \bar{D} and Re on deposition	30
4.3	Deposition for the entire lung-specific Re range	36
5	Deposition Modelling	39
5.1	Model development	39
5.2	Deposition calculation using the Model	43
6	Conclusion and Future Scope	48
6.1	Conclusion	48
6.2	Future scope	49
A	MATLAB code for global pdf	50

LIST OF TABLES

1.1	Dimension of each generations of lungs (Weibel <i>et al.</i> , 1963)	4
3.1	A table listing bronchiole diameter as a function of the branching generation in the lung. Typical Re is calculated based on tidal volume of 500ml and a 4s breathing cycle.	18
3.2	Optical settings of PDPA	24
4.1	Definition of dimensionless parameters	29
4.2	Uncertainty in the measured and calculated parameters.	30

LIST OF FIGURES

1.1	Schematic of human lung morphology proposed by Weibel et al. (1963) . The schematic shows the conducting and acinar airways. The conducting airways transports air from nose and mouth to lungs through trachea whereas the acinar airways consists of alveolar ducts that participates in gaseous exchange with blood.	2
1.2	Plot showing the variation of the total cross sectional area of the lung airways for different generations. The diameter of the airways decreases continuously as the number of generation increases, but the branching of airways at each generation causes the total cross sectional area to increase enormously for $G > 16$, which is identified as <i>respiratory zone</i>	3
1.3	Plot showing the variation of Reynolds number (Re) for different generations. Considering tidal volume of the lungs to be 500 ml and one breathing cycle to be of 4 sec (inspiration: 2 sec ; expiration: 2 sec), the Re is $\sim \mathcal{O}(10^3)$ in trachea and $\sim \mathcal{O}(10^{-1})$ in alveoli.	5
1.4	Plot showing the death and disability adjusted life years of the global population due to respiratory diseases like tuberculosis, trachea / bronchus / lung cancer, chronic obstructive pulmonary disease (COPD), lower respiratory infections. The figure shows that about 9.5 million peoples died and 154 million people suffering from DALYs due to these respiratory diseases (report till 2008; source: World Health Statistics 2011 by WHO).	6
1.5	Plot showing the death rate due to chronic respiratory diseases in India and world wide for the period of 1990 - 2017. The average death rate in India is about 90.5 per 100,000 which is much higher than the global death rate of 55.03 per million (Source: Global Burden of Diseases)	7
2.1	Figure showing Scanning Electron Microscope image of a section of human lung parenchyma. A - alveolus; S - alveolar septa; D - alveolar duct; PK - pore of Kohn; PA - small branch of the pulmonary artery. Source: Levitzky (2007) ; West (2012)	12
3.1	Schematic of the experimental setup consisting of aerosol generator, micro-capillary (phantom bronchiole), syringe with a motor arrangement to draw the plunger at a constant velocity. The inlet of the bronchiole is placed at a height of 5mm above the geometric center of the nebulizer exit. Different flow conditions through the micro-capillaries were achieved by controlling the rotational speed of the 12V DC motor using a 32V , 2A DC power supply.	19

3.2	Images of vials (a) containing a solution with freshly prepared Boron doped Carbon Dots (BCD) and (b) showing emission of blue light by BCD when excited by ultraviolet light of wavelength $350nm$	20
3.3	(a) Transmission Electron Microscopy (TEM) image of Boron doped Carbon Quantum Dots. Scale is indicated as a white bar. (b) Histogram of the size distribution of BCD estimated from the TEM images. The BCD distribution is nearly mono-disperse.	21
3.4	Plot of droplet size distribution for Omron [®] make jet nebulizer, mesh nebulizer, JICF (Mallik <i>et al.</i> , 2020) and solid cone spray (Make: Delevan [®]). In the figure it is evident that the size distribution of the spray and JICF spans a wide range of diameters where as the distribution of the nebulizers is comparatively mono dispersed.	23
3.5	Schematic of measurement location of drop size and velocity, $5mm$ above the nebulizer exit, using Phase Doppler Particle Analyzer . . .	24
3.6	Plot of (a) the global diameter probability distribution function and (b) the global velocity probability distribution function, both measured using PDPA. The most probable drop size of size $6.5\mu m$. Most drops were moving at a velocity less than $0.5ms^{-1}$ indicating that the aerosol plume was finely atomized and gently rising, as desired.	25
3.7	Bar plot showing concentration (α_0) of the generated drop for jet nebulizer, mesh nebulizer, JICF and solid cone spray. Among all, mesh nebulizer is found to have lowest droplet concentration of 6.26×10^{-5} that confirms the aerosol plume to be dilute and non - interacting. . .	26
4.1	Plot of (a) variation of deposition fraction per unit capillary length per unit time (\overline{D}_F) with capillary length (L) and (b) the variation of dimensionless deposition (δ) versus aspect ration (\overline{L}), for different Reynolds number (Re). The data shows an inverse relation of δ with bronchiole aspect ratio (\overline{L}). For high \overline{L} , the effect of Re is negligible.	32
4.2	Plot of (a) deposition fraction per unit capillary length and unit time (\overline{D}_F) with tubules diameter (D) and (b) dimensionless deposition (δ) versus dimensionless bronchiole diameter (\overline{D}), for varying bronchiole aspect ratio (\overline{L}). Reynolds number was constant at $Re = 512$. The tubules diameter mimics $7^{th} - 23^{rd}$ generation of the lungs. It is seen that with increase in \overline{D} the dimensionless deposition (δ) increases, while \overline{L} still follows the inverse relation with δ for a constant \overline{D}	33
4.3	Plot of (a) deposition fraction per unit capillary length and unit time (\overline{D}_F) with tubules diameter (D) and (b) dimensionless deposition (δ) versus \overline{D} for varying particle-based Reynolds number ($Re\overline{D}$), keeping aspect ratio $\overline{L} = 100$. It is seen that δ increases with \overline{D} . $Re\overline{D}$ does not affect the deposition.	35

- 4.4 (a) Plot of \overline{D}_F versus Re . Re varies over five orders of magnitude of mimicking flow conditions in different generations of the lung. The deposition fraction per unit tubule length and per unit suction time represented by D_F shows the lowest value when $Re = 1$, for $\overline{L} = 50$ and 150. According to the deposition mechanism of aerosols three zones are identified as follows: deposition by *impaction* ($10 < Re \leq 10^3$), deposition by *sedimentation* ($10 < Re < 1$), deposition by *diffusion* ($10^{-3} \leq Re < 1$). (b) Plot of $\delta\overline{L}$ versus Re for \overline{D} being constant at 77 and for $\overline{L} = 50$ and 150. Re varies over five orders of magnitude. The data in figure 4.4 (a) collapses onto a single curve when re-scaled as above. Interestingly, $\delta\overline{L} \sim Re^{-2}$ for $Re < 1$ and is constant for $Re > 1$. In the plot green dotted line is the best fit for $Re < 1$ given by $\delta\overline{L} = 1.55 \times 10^{-7} Re^{-2}$. Blue dotted line is the best fit for $Re > 1$ given by $\delta\overline{L} = 2.73 \times 10^{-7}$. Figure legend: \triangle Kim *et al.* (1984); \blacktriangleleft Matsui *et al.* (1974); \square Tao *et al.* (2018); \star Ström (1972) 38
- 5.1 (a) Modified representation of figure 4.3(b). The same data is re-plotted to show the variation of $\delta\overline{L}$ versus \overline{D}^3 . The best fit power law is given by $\delta\overline{L} = 7 \times 10^{-13} \overline{D}^3$. The fit is independent of $Re\overline{D}$. $Re \sim 10^3$ for all data in these plots implying impaction-dominated deposition. (b) Modified representation of figure 4.4(b) where $\delta\overline{L}$ is plotted against particle Reynolds number ($Re\overline{D}$ instead of flow Re). The best fit represented by green dotted line is given by $9 \times 10^{-4} (Re\overline{D})^{-2}$ 41
- 5.2 (a) Plot of deposition fraction (D_F) versus lung generations (G) calculated from equation 5.1 for particle size $\sim \mathcal{O}(10\mu m)$ and breathing cycle of 4s. (b) Variation of deposition fraction with particle diameter given by Hinds (1999). The plot shows that for particle diameter of 10 micron the total deposition fraction is 83%, out of which 2% is deposited in alveolar and tracheobronchial region and remaining in the upper airways. This results matches well with model predicted deposition in plot (a) 42
- 5.3 Plot of deposition fraction (D_F) and generation number, calculated using equation 5.1 for single breathing cycle (4s) and particle size $\sim \mathcal{O}(10\mu m)$ The plot is same as figure 5.2(a) with the abscissa in the log scale. The discontinuity of the plot after $G = 11$ is due to the change in deposition model from equation 5.1(a) to (b) resulted due to the change in Re 43
- 5.4 (a) Plot of D_F and lung generations (G) for different breathing frequency. The time for each breathing cycle is considered as time for inspiration and expiration together. (b) Plot of D_F and G for different breath hold time. For both the plots it can be seen that model for $Re \gg 1$ do not show any response with breathing frequency and breath hold time, whereas the model for $Re \ll 1$ found to be very sensitive for both of these parameters. 46

5.5 Plot of variation of alveolar deposition fraction (D_F) with time for different breathing frequency and breath hold time. The alveolar D_F scales to T^2 for breathing cycle (Blue dotted line: $D_F = 0.04T^{1.96}$ and scale to T for breath hold time (Red dotted line: $0.766T^{1.16}$) 47

ABBREVIATIONS

COPD	Chronic Obstructive Pulmonary Disease
WHO	World Health Organisation
DALY	Disability Adjusted Life Years
pMDI	Pressurised Meter Dose Inhaler
DPI	Dry Powder Inhaler
PIV	Particle Image Velocimetry
PTFE	Polytetrafluoroethylene
CD	Carbon Quantum Dots
QY	Quantum Yield
BCD	Boron doped Carbon Quantum Dots
TEM	Transmission Electron Microscopy
PDPA	Phase Doppler Particle Analyzer
PMT	Photo Multiplier Tube
JICF	Jet in Cross Flow
<i>pdf</i>	Probability Density Function

NOTATION

G	Lung Generation
d	Measured aerosol deposition, (ml)
L	Length of bronchiole, (mm)
D	Bronchiole diameter, (mm)
Q	Volume flow rate, (ml/s)
T	Time duration of the flow, (s)
ν	Kinematic viscosity of air, (m^2/s)
D_{10}	Mean droplet diameter, (μm)
α_0	Volume fraction of aerosol from nebulizer, (ml of aerosol per ml of space)
D_F	Deposition Fraction
\overline{D}_F	D_F per capillary length per unit time
\overline{L}	Aspect ratio
\overline{D}	Dimensionless bronchiole diameter
\overline{T}	Dimensionless Time
Re	Flow Reynolds number
Re_p	Particle Reynolds number
δ	Deposition fraction per dimensionless length per dimensionless time

CHAPTER 1

INTRODUCTION

The transport and deposition of aerosols in human lungs has attracted enormous attention from modern researchers for its application to pulmonary drug delivery and to minimise the adverse effect of atmospheric pollutants on human health. This chapter discusses the morphology of human lungs and breathing mechanisms, along with the transportation mechanics of aerosol particles in the lung airways. The objective and the scope of the study is discussed by highlighting the motivation for this study. Lastly, the overview of this thesis is presented in this chapter.

1.1 Lung Morphology

The human respiratory system comprises of (i) *The upper respiratory tract* consisting of the nose, nasal passages, mouth, larynx, pharynx and trachea and (ii) *The lower respiratory tract*, consisting of lungs. The human pulmonary system consists of left and right lungs, divided into slightly unequal proportions and connected to the upper respiratory system by the trachea. The architecture of the human lungs consists of a branching network through a sequences of bifurcation, known as bronchi. The diameter and length of the bronchi changes at each level of bifurcation, known as generation (G), starting with trachea as $G = 0$. A model for the morphological structure of the lung was proposed by Weibel *et al.* (1963) where he presented a qualitative and quantitative description of the bronchial tree as shown in Figure 1.1, consisting of 23 levels of bifurcation or generations. Thus each half of the lungs has $2^{23} = 8388608$ airway tubes. The trachea ($G = 0$) supplies air to these 2^{23} ducts from the nose and mouth. The airways in the tracheobronchial region, i.e. $G = 0 \rightarrow 16$, only conduct the flow of gases in and out from the lungs and do not participate in the gaseous exchange between the bloodstream and air. Thus, they constitute the anatomic dead space, approximately of volume 150 ml. In the pulmonary region, i.e. $G = 17 \rightarrow 19$, the wall of airways are lined with air-exchange sacs, known as alveoli, which are the respiratory bronchioles. The alveoli

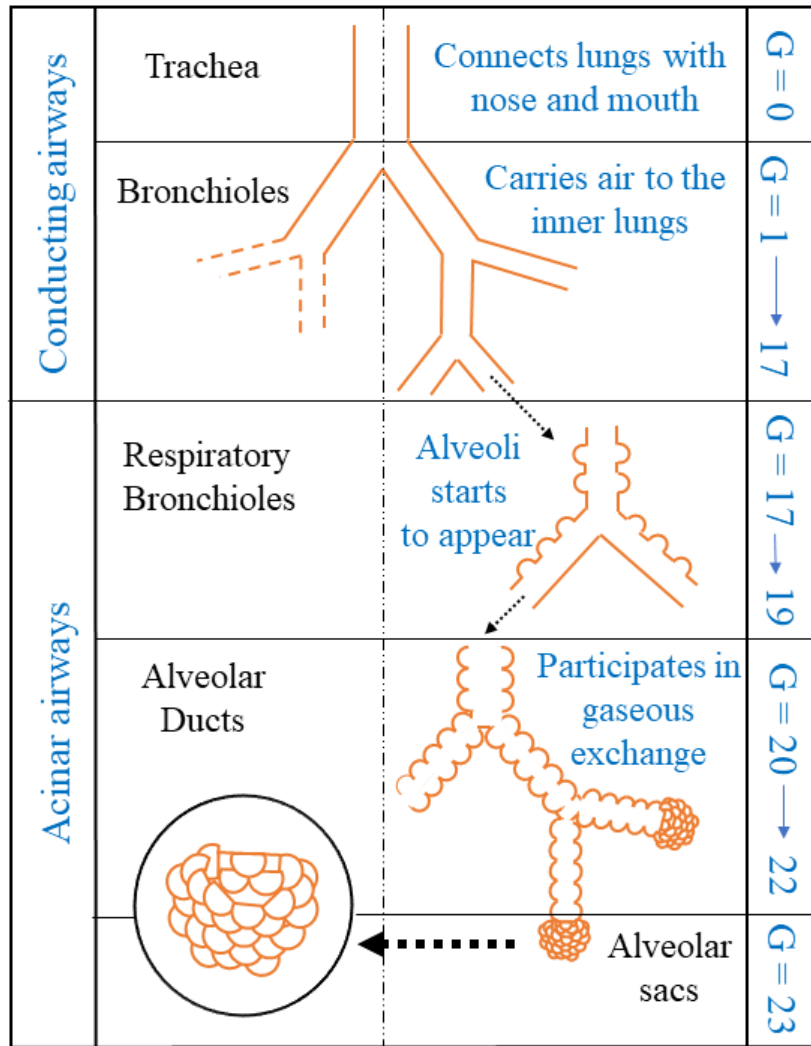


Figure 1.1: Schematic of human lung morphology proposed by [Weibel et al. \(1963\)](#). The schematic shows the conducting and acinar airways. The conducting airways transports air from nose and mouth to lungs through trachea whereas the acinar airways consists of alveolar ducts that participates in gaseous exchange with blood.

are facilitated with capillary blood supply and can exchange gases between the inhaled air and bloodstream. For generations $G = 20 \rightarrow 23$, known as the respiratory zone, the airways are completely made up of alveoli where $G = 23$ consists of clusters of alveoli. This zone consists of most of the lung volume which is about 2.5 to 3 *liters*. There are about 300×10^6 alveoli each of having diameter of $\sim 300 \mu\text{m}$ in each human lung ([West, 2012](#)). Considering the alveoli to be of spherical shape the total surface area is estimated to be around $\sim 85 \text{ m}^2$ which is more than the area of a badminton court although their total volume is only about 4*l*. While $G = 0 \rightarrow 16$ participate in conduction of air to lungs, $G = 17 \rightarrow 23$ participate in exchanges of gases between blood and inhaled air ([Grotberg, 2011](#)).

1.2 Breathing Mechanism

The respiration process is governed by the expansion and contraction of the diaphragm and the intercostal muscles. At the time of inspiration, the contraction of diaphragm raises the ribs, thus increasing the volume of the thoracic cavity as a result of which air is drawn into the lungs. The inspired air flows through the airways, up to the terminal bronchioles ($G = 16$) without any gaseous exchange with blood. Beyond $G = 16$, the total cross section area of the airways increases enormously (ref. Figure 1.2) due to the branching of bronchioles and the velocity of air becomes very small. In the last

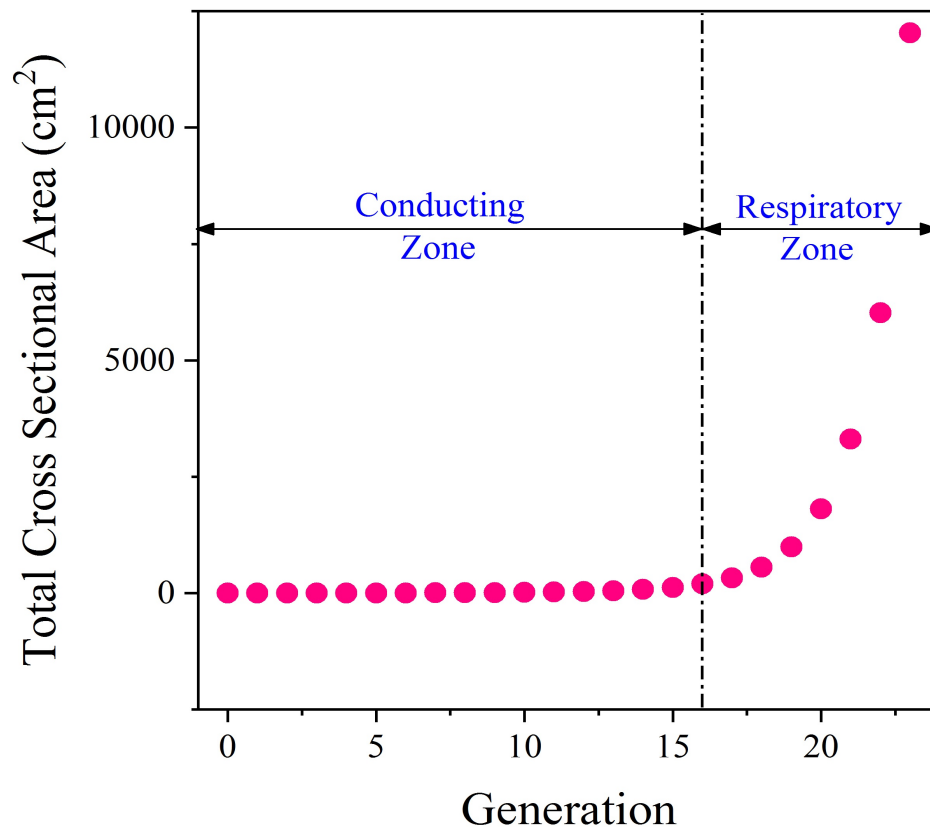


Figure 1.2: Plot showing the variation of the total cross sectional area of the lung airways for different generations. The diameter of the airways decreases continuously as the number of generation increases, but the branching of airways at each generation causes the total cross sectional area to increase enormously for $G > 16$, which is identified as *respiratory zone*.

few generations, the air velocity becomes so less that diffusional mechanism becomes dominant. The tidal volume of human lungs is about 500 ml which requires a low distending pressure of approximately 3 millibar , which is about 10 times lesser than the pressure required to inflate a rubber balloon of the same volume.

1.3 Transport of Aerosol Particles in Lungs

The length and diameter of the airways varies enormously from generation to generation in the lung, starting with tracheal diameter of 18 *mm* to 0.41 *mm* at alveoli, as measured by Weibel *et al.* (1963). The lung dimensions are given in Table 1.1. This variation of

Table 1.1: Dimension of each generations of lungs (Weibel *et al.*, 1963)

Genetations (G)	Number of Branches 2^G	Diameter (cm)	Length (cm)
0	1	1.8	12
1	2	1.22	4.76
2	4	0.83	1.9
3	8	0.56	1.76
4	16	0.45	1.27
5	32	0.35	1.07
6	64	0.28	0.9
7	128	0.23	0.76
8	256	0.186	0.64
9	512	0.154	0.54
10	1024	0.13	0.46
11	2048	0.109	0.39
12	4096	0.095	0.33
13	8192	0.082	0.27
14	16384	0.074	0.23
15	32768	0.066	0.2
16	65536	0.06	0.165
17	131072	0.054	0.141
18	262144	0.05	0.117
19	524288	0.047	0.099
20	1048576	0.045	0.083
21	2097152	0.043	0.07
22	4194304	0.041	0.059
23	8388608	0.041	0.05

airway diameter by about 4 orders of magnitude ($\sim O(10^2)$ at $G = 0$; $\sim O(10^{-1})$ at $G = 23$), causes a huge variation of air velocity an thus the Reynolds number (Re). The order of Re varies several orders of magnitude over different generations as shown in Figure 1.3, starting from $\mathcal{O}(10^3)$ in trachea to $\mathcal{O}(10^{-2})$ in alveoli, based on tidal volume of lungs to be 500 ml per inspiration of 2 seconds and kinematic viscosity of air at STP. This variation of air velocity gives rise to several deposition mechanism, such as deposition by *impaction*, *sedimentation* and *diffusion*. For very high Re and

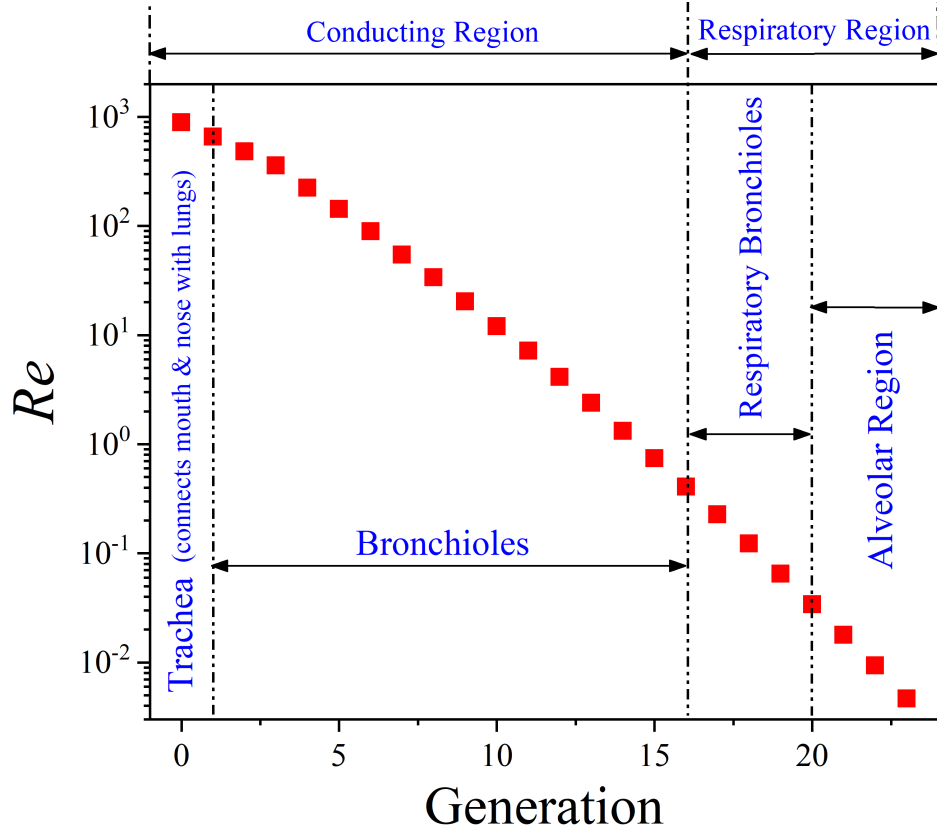


Figure 1.3: Plot showing the variation of Reynolds number (Re) for different generations. Considering tidal volume of the lungs to be 500 ml and one breathing cycle to be of 4 sec (inspiration: 2 sec ; expiration: 2 sec), the Re is $\sim \mathcal{O}(10^3)$ in trachea and $\sim \mathcal{O}(10^{-1})$ in alveoli.

large particles, the particles are offset from the air particle trajectory due to inertia and hit the wall of the airways which causes deposition due to *impaction*. This kind of deposition mainly at the upper generation of lungs where $10 \leq Re \leq 10^3$. The deposition by *sedimentation* occurs where Re is relatively low, $1 < Re < 10$, when the gravitational force dominates over the inertia of the particles. *Diffusion* occurs mainly due to Brownian motion of the particles at very low Re , ($10^{-2} \leq Re \leq 1$) and for small particles. The diffusion dominated deposition in the last few generation of lungs where the airway passages are extremely small and air flow velocity is negligible.

Extrathoracic deposition is also a major cause of particle loss in the pulmonary system. The 90° bend geometry of the mouth and throat causes major fraction of the nebulized drug to deposit in that region, although the large particles are filtered out in the nose. The deposition of the smaller particles occurs in the conducting airways and are removed by a moving staircase of mucus that sweeps up the deposited particles to the epiglottis, where it is swallowed. The particles that deposit in the alveoli are engulfed

by large wandering cells called macrophages. The flow of blood removes the foreign materials from the lungs and blood cells and poses a defense to them [West \(2012\)](#).

1.4 Motivation

Death that occurs by infection in the lower respiratory system, chronic obstructive pulmonary disease (COPD) and tracheal / bronchial cancer comprise of 17% of the global death (Source: [World Health Organisation; WHO](#)). The Global Burden of Disease study reported 251 million cases of COPD globally during the year 2016 which makes such respiratory diseases a matter of great concern. The effect of respiratory diseases

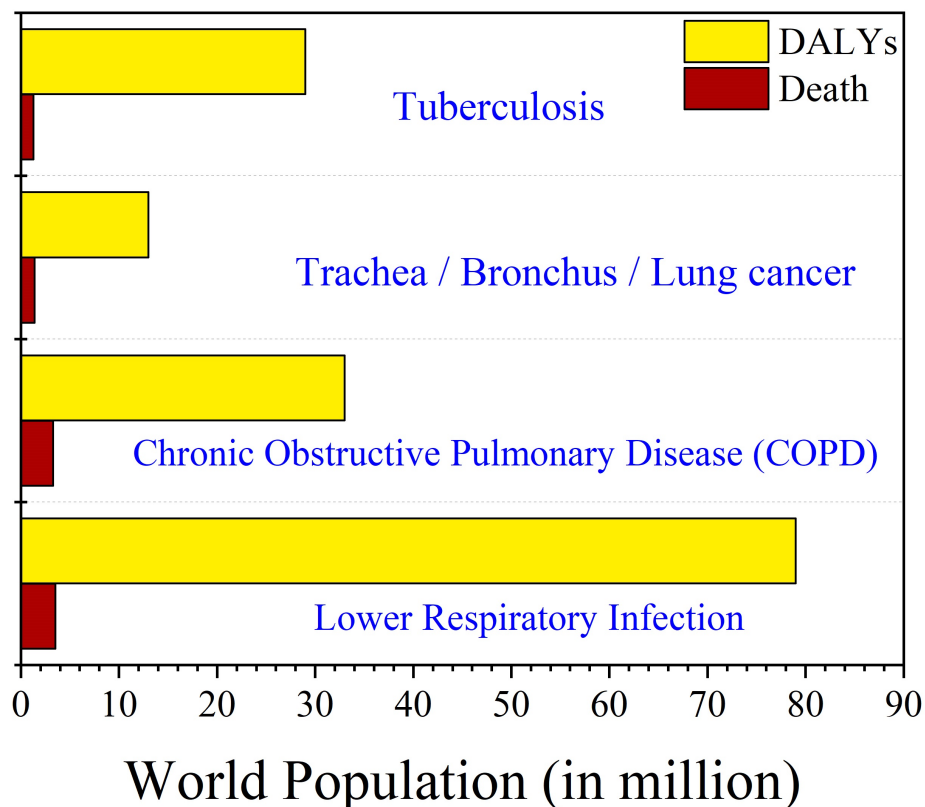


Figure 1.4: Plot showing the death and disability adjusted life years of the global population due to respiratory diseases like tuberculosis, trachea / bronchus / lung cancer, chronic obstructive pulmonary disease (COPD), lower respiratory infections. The figure shows that about 9.5 million peoples died and 154 million people suffering from DALYs due to these respiratory diseases (report till 2008; source: [World Health Statistics 2011 by WHO](#)).

on global population is shown in Figure 1.4, which caused death of 9.5 millions and disability adjusted life years (DALYs) of 154 million (report till 2008; source: [World Health Statistics 2011 by WHO](#)). For the period of 1990 - 2017, the average death rate

due to chronic respiratory disease in India is about 90.5 per million, much higher than the global death rate which is around 55.03 per million (Ref: Figure 1.5; source: [Global Burden of Diseases](#)). Investigation of aerosol deposition and particle transport in lungs can pave the way for health risk assessment due to the presence of atmospheric particulate matter and to assess the effectiveness of systemic drug delivery which is the main motivation behind this study.

The lung airways are often used as a route for treatment of various respiratory diseases since it provides rapid and non-invasive drug transfer to blood stream. The conventional treatment of lung disease rely on nebulized drug in the form of powder or liquid drop, which is targeted to the pulmonary and alveolar region of lungs since their large surface area provides rapid mixing of drug with the blood and avoids first pass metabolism. Thus, estimation of particle deposition helps in gauging the effectiveness of the drug delivery along with assessing the spreading of infections through inhalation.

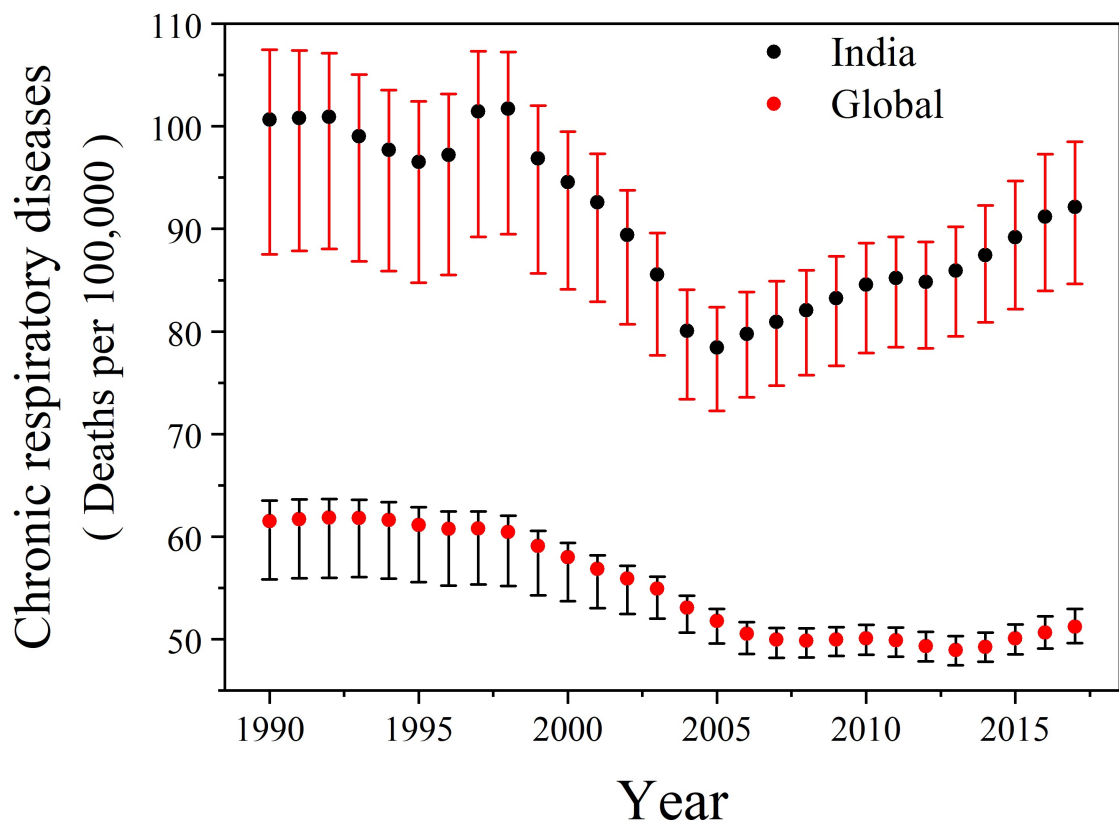


Figure 1.5: Plot showing the death rate due to chronic respiratory diseases in India and world wide for the period of 1990 - 2017. The average death rate in India is about 90.5 per 100,000 which is much higher than the global death rate of 55.03 per million (Source: [Global Burden of Diseases](#))

Despite significant progress in quantifying particle deposition, both experimentally and numerically, there are still several discrepancies among the researchers regarding the fraction of the inhaled drug that actually reaches the pulmonary region. The drug delivery efficiencies for pressurised meter dose inhaler (pMDI) and dry powder inhalers (DPI) is approximately 40% - 60% (Clark, 2004), where the efficiencies for soft mist inhalers increase up to 80%, although their pulmonary deposition is not reported. According to Kleinstreuer and Zhang (2010) the delivery efficiencies of current inhalers is 10% - 30% for adults and 3% - 15% for children. Again Deng *et al.* (2019a) showed that the deposition of particles in upper, middle and lower lungs varies with breathing rates that vary with various physical activities such as sedentary activities (sitting, lying down etc), moderate activities (walking, cycling etc) and intense activities (running, hiking, swimming etc). Moreover, most of the numerical studies are restricted up to few generations in the upper, middle or lower lung due to the limitation of the computational power and time. On the other hand, experimental deposition studies are restricted to nose, throat, few generations in upper lungs or scaled up version of inner lungs due to its complex and miniaturized geometry. Since the deposition in pulmonary and acinus region decides the response of the drug and its delivery efficiency, it is necessary to estimate deposition fractions in inner lungs experimentally in true scale models and thereafter validate numerical results.

From an engineering point of view, human lungs is an excellent natural device to study as it generates a wide range of flow conditions starting from $Re = 10^3$ to $Re = 10^{-2}$. This provides an opportunity to study different flows such as turbulent flow in the upper airways, laminar flow in mid airways and creeping flow in lower airways and their effects on particle transport as well as deposition. Thus the necessity of detailed experimental study and the elegance in the physics that is observed in a single human organ motivates and inspires this work.

1.5 Objectives

While the primary purpose of the respiratory system is to enable gas exchange, it also provides a route for pulmonary aerosol transport. The constant variation of airway diameter causes a huge change in Re , over five orders of magnitude in every single breath.

Since different fluid mechanic conditions give rise to various deposition mechanisms, it is necessary to be able to quantify the total lung deposition along with the regional depositions. The deposition in distal alveolated region seeks attention for quantifying disease propensity as well as therapeutic efficacy. The objective of this proposed work are:

- i. To study the effect of bronchiole diameter and aspect ratio, mimicking the lung airways, on aerosol deposition.
- ii. To study the effect of particle Reynolds number (Re) on deposition of aerosols.
- iii. To quantify the amount of deposition for different orders of Re , starting from $Re \sim \mathcal{O}(10^3)$ (in tracheal region) to $Re \sim \mathcal{O}(10^{-2})$ (in alveolar region).
- iv. Finally, to develop a universal bronchiole scale deposition model, which can form the building block for estimating the total aerosol deposition in lungs.

1.6 Overview of the thesis

The thesis is designed to start with a brief introduction on lung morphology and thereafter discussing the experimental techniques used to quantify the deposition of aerosols in phantom bronchioles. The effect of several parameters like capillary diameter, aspect ratio, Reynolds number (Re) etc. on aerosol deposition is discussed in detail in this thesis. Finally, this study ends with developing a universal bronchiole scale deposition model which can estimate the total aerosol deposition in lungs. The chapters in the thesis are organised as follows:

Chapter 2 outlines a survey of the literature on numerical and experimental studies related to deposition of aerosols. The regional and total deposition studies present in the literature (both numerical and experimental) are discussed. The regional deposition studies that are discussed in this chapter contain deposition in mouth/throat, deposition in upper lungs and deposition in lower lungs. Lastly, the gap in the existing literature is stated clearly, indicating the necessity of this study.

Chapter 3 includes the detailing of the materials used for this experimental study.

Chapter 4 discusses the experimental methods used for this study. The first part of this chapter gives a detailed description of the experimental setup. The chapter also discusses the characterisation of the aerosol particles and measurement of aerosol con-

centration. The end of the chapter highlights the method for analysis of deposition samples.

Chapter 5 discusses a presentation of the experimental results and their non-dimensional counter parts. The first part of this chapter deals with the non-dimensionalizing the parameters varied in the experiment, highlighting the uncertainties associated with them. The later part of the thesis discusses the effect of those dimensionless parameters on deposition of aerosols.

Chapter 6 proposes a universal bronchiole scale deposition model for estimating total deposition in the lungs which is developed from the experimental data.

The key results obtained from this study is concluded in **Chapter 7**. This chapter also includes the scope of continuing this work in future based on deposition study in branched capillary instead of straight tubules.

CHAPTER 2

Literature Survey

Aerosol deposition in lungs has attracted the attention of the researchers for several decades, one of the reasons being to understand the complicated nature of aerosol transport in lung airways. Since the lung provides a viable drug delivery route, researchers are keen to predict the regional drug deposition to estimate drug efficacy. Besides this, researchers have also paid attention to the transport of the atmospheric pollutants to regulate health effects. This chapter starts with a brief introduction to the studies carried out to estimate lung morphometry. The later sections of the chapter discuss the existing literature on aerosol deposition in the throat, upper lungs and lower lungs along with the deposition models developed by the researchers.

2.1 Determination of lung morphometry

A preliminary model of lung geometry and dimensions was given by [Weibel *et al.* \(1963\)](#), followed by various studies reporting lung morphometry ([Horsfield and Cumming, 1968](#); [Phalen and Oldham, 1983](#); [Yeh *et al.*, 1976](#)). These researchers estimated the length, diameter and angle of bifurcation at every generation using silicon rubber casts of dissected mammalian or cadaver human lungs ([Horsfield and Cumming, 1968](#); [Yeh *et al.*, 1976](#); [Phalen *et al.*, 1978](#)). The morphometric dimensions of the bronchial tree as reported by [Horsfield *et al.* \(1971\)](#) is restricted to diameters below 0.7mm and no attempt was made to find the mean pathway of the lungs. A detailed measurement study was later reported by [Raabe \(1976\)](#). This study consists of data pertaining to the length, diameter and bifurcation angles starting from trachea to the terminal bronchioles. But their study is restricted to 10% – 25% of the bronchioles, which makes the acinar structure somewhat incomplete. Morphometry data in the acinar region is very sparse in the literature due to its small dimensions. One of the first acinar measurements was given by [Hansen and Ampaya \(1975\)](#), which completes the respiratory model and is now widely used.

A realistic lung model with proper dimensions is required to study aerosol deposition, as the bronchial tree model may play a role in determining drug delivery efficiency (Mauroy *et al.*, 2004). The above studies assume that the measured fraction of the airways always represent the fraction of missing airways (Hofmann *et al.*, 2008). Thus, these studies have contributed to the development of a *symmetric deterministic model* or *typical path model*. A few studies reported *asymmetric* or *multi path models*, which were developed by combining the stochastic paths for the missing lower airways with symmetric models (Asgharian *et al.*, 2001; Hofmann *et al.*, 2008). Hofmann and Koblinger (1990) used diameter frequency distribution and different correlations between parent and daughter airways to develop multi-path models. Figure 2.1 shows an

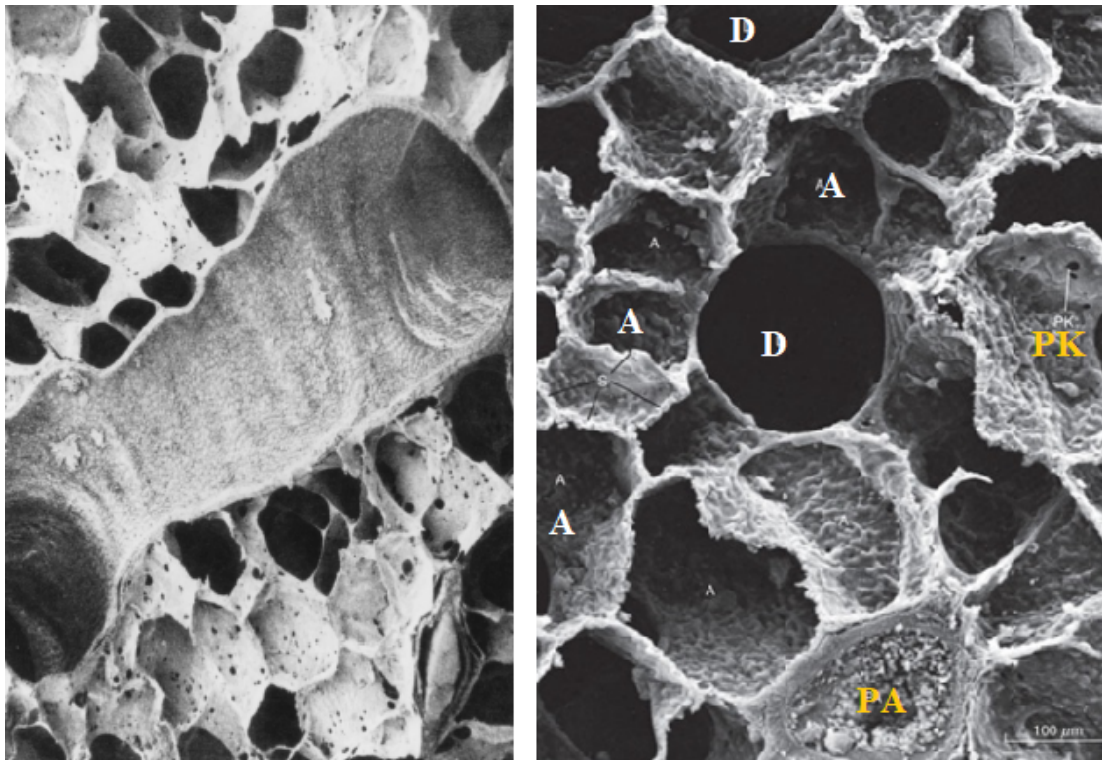


Figure 2.1: Figure showing Scanning Electron Microscope image of a section of human lung parenchyma. A - alveolus; S - alveolar septa; D - alveolar duct; PK - pore of Kohn; PA - small branch of the pulmonary artery. Source: Levitzky (2007); West (2012)

electron microscopic image of a section of the human lungs, showing the small bronchioles and alveoli. It gives a good pictorial representation of the structure and dimension of respiratory bronchioles, alveolar ducts and alveolar sacs.

2.2 Deposition studies on throat model

While morphometry has been the focus of a large body of literature, the objective of these studies is to understand breathing and aerosol deposition for therapeutic use. It is necessary for the inhaled drug to reach the pulmonary region of the lungs to show its remedial effects. However, a major fraction of the nebulized drug deposits in the mouth and throat due to its 90° bend geometry, which is a matter of great concern. The momentum of aerosol significantly gets affected by mouth and throat geometry which causes significant amount of deposition in that region (Longest *et al.*, 2008). The deposition efficiency in the throat region when correlated with initial parameters like droplet size and flow rates, indicates that the inertial impact is the dominant deposition mechanism. Additionally, the inhaler geometry also plays a significant role in deposition in the throat and mouth (DeHaan and Finlay, 2001). An elaborate study was done by the researchers on the deposition of aerosols with an idealized human throat model. The numerical studies of aerosol deposition (Li and Edwards, 1997) showed that the deposition in the throat increases with particle diameter. The experimental results for deposition of poly-dispersed aerosol in human throat replica showed good agreement with numerical results generated by $k-\epsilon$ model (Stapleton *et al.*, 2000). But the PIV study on molded throat model by Jayaraju *et al.* (2008) showed good validation with DLS and LES rather than $k-\omega$ RANS model. The deposition for in vivo human throat showed a deposition of 40% for $1\mu m$ particles and of 80% for $10\mu m$ particles. Effect of Stokes number and flow Reynolds number were examined using gamma scintigraphy and gravimetry for extrathoracic deposition of aerosol using the idealized human mouth and throat replica by Grgic *et al.* (2004). Their study showed the aerosol to be deposited mostly in the larynx and trachea. However, the total deposition was observed to be independent of mouth-throat geometry. It was observed the deposition fraction is largely dependent on inertial parameters, indicating impaction dominated deposition mechanism (Grgic *et al.*, 2004).

2.3 Deposition studies in the upper lung

A significant number of experimental and numerical studies have been focused on aerosol deposition in upper lungs to understand the flow physics and deposition mechanism in airway branching. [Deng et al. \(2019a\)](#) investigated deposition of atmospheric particulates within a one-dimensional numerical trumpet model of lung. They concluded that particles of size $> 2.5\mu m$ deposit mainly in the tracheobronchial region of the lungs which reduces the pulmonary deposition. The deposition varies heavily with the breathing rate or with the type of activities ([Deng et al., 2019b](#)). The particle deposition is uniform among different generations for moderate activity, more in lower airways (14 - 16 generations) during sedentary activities and greater in upper airways (3 - 5 generations) during intense activity. This heavy deposition of particulates in tracheobronchial airways can cause different health effects for a person undergoing different activities throughout the day. The photo-metric measurement of inhaled and exhaled iron oxide particles of $1\mu m - 10\mu m$ by [Stahlhofen et al. \(1980\)](#) showed similar result where the deposition is high in the thorax. The study of [Bennett et al. \(2019\)](#) included the effect of lung tidal volume and inspiratory to expiratory ratio along with the breathing rate. Their study shows an increase in aerosol deposition with tidal volume, breathing rate and inspiratory time. They concluded that breathing frequency is not the only factor responsible for heavy deposition in the tracheobronchial region. The numerical study of [Chakravarty et al. \(2019\)](#) showed that the increase in breathing frequency enhances the transport rate of aerosol and it is further enhanced when the particle size is reduced. External forces such as gravity and inertia act on inhaled particles causing non-uniform deposition of aerosols in lung airways. [Asgharian and Price \(2006\)](#) The heterogeneous pattern of aerosol deposition in the trachea and bronchus changes with types of nebulizer among which mesh nebulizer is found to be most efficient for drug delivery to the bronchus ([Xi et al., 2018](#)).

A detailed understanding of airflow throughout the lungs is required to locate vulnerable sites of particle deposition and to target specific regions of the lungs with inhaled drugs more efficiently. The transition and the turbulence regime of airflow have a significant effect on localized particle deposition for bifurcating respiratory model. The investigation of [Longest and Vinchurkar \(2007\)](#) showed that even though Reynolds

number (Re) is below the critical limit required for full turbulence, the transitional characteristics and turbulence has a great influence on the flow field and local particle deposition patterns. The experimental determination of aerosol deposition within the lung of human subject or lung model is restricted to the total deposition of aerosol (Lizal *et al.*, 2015) for most of the cases although it is not a good indicator of inter-subject variability (Devi *et al.*, 2016). Researchers have reported in vivo results for inhaling either through mouth or nose for a wide range of particle sizes and flow rates. (Heyder *et al.*, 1986) The total deposition of aerosols in the lungs increases with an increase in particle size and flow rate (Darquenne *et al.*, 2016) which concludes that the deposition in a given region in the lungs is directly proportional to the volume of air delivered to that region (Asgharian and Price, 2006; Asgharian *et al.*, 2004).

2.4 Deposition study in deep lung model

The knowledge of aerosol deposition in deep lung is essential in view of advanced strategies of drug targeting, since alveolus provides the communication between the inhaled air and the blood stream (Semmler-Behnke *et al.*, 2012; Kleinstreuer *et al.*, 2008). A large number of computational studies conducted over past decades provided in-depth understanding of acinar flows and their intrinsic complexities. The acinar flow plays a critical role in influencing the kinematics of inhaled particles. Thus a detailed knowledge of acinar flow phenomena is required in characterizing aerosol deposition in the acinar region (Sznitman, 2013) as anisotropic wall motion of the acinar airways may influence deposition in deep lung (Hofemeier and Sznitman, 2016). The numerical simulation shows enhancement of particle transport rate due to a reduction in particle size, which signifies that diffusion mechanism dominates over advection in the acinar region (Chakravarty *et al.*, 2019). As diffusion is a slow process, the breath holding time plays a significant role in alveolar deposition (Khajeh-Hosseini-Dalasm and Longest, 2015). The numerical study of Koullapis *et al.* (2018) shows particles of size 1 – 5 μm have the highest possibility of deposition in the acinar region since they remain suspended and sediment during the early stage of exhalation. Thus for effective drug delivery one should give a long pause after inhalation, so that the deposition of the drug increases in the acinar region (Koullapis *et al.*, 2020).

Most of the experimental studies available in the literature are restricted to the upper generation of lungs. Deposition studies in the deep lung (i.e. $G = 20 \rightarrow 23$) are rare due to its micro-scale dimensions and complex geometry. The real time visualization of particle dynamics in real lung is also unavailable due to lack of appropriate experimental techniques. With the advent of micro-fluidics (Baker, 2011; Esch *et al.*, 2011; Huh *et al.*, 2010; Moraes *et al.*, 2012), some insights on acinar deposition are obtained but the results in physiologically realistic acinar environment is still rare (Sznitman, 2013). The very small flow rate in acinar region and the micro size of the airways makes it difficult to mimic the corresponding flow conditions for experimental study. Among the few experimental studies in the existing literature, the experimental results on true scale acinar model by Fishler *et al.* (2015) shows a good agreement with numerical data. The bifurcated alveolar ducts that have breathing like wall motion to capture respiratory flows in acinus but it is restricted to constant diameter bifurcations although the variation in diameter have significant effect in deposition. Similarly, Lin *et al.* (2019) investigated with bifurcated tubules of differing diameter and low Re (between 0.1 and 1), but the study is restricted to a few generations of the lower lung that does not completes the acinar deposition model. The convective mixing of the particles found to be maximum near alveolar openings where the streamlines are slow and are prone to deposition (Fishler *et al.*, 2017).

While different deposition mechanisms are activated in different regions of the lung owing to differing fluid mechanic conditions, it is important to be able to quantify the total amount of aerosol deposited in the lung (Devi *et al.*, 2016; Lizal *et al.*, 2015) as well as deposition by region (Ferron, 1977; Stahlhofen *et al.*, 1980). Since inhalation therapy finds application in the treatment of various lung disorders such as asthma, chronic obstructive pulmonary disease (COPD), respiratory infection, lung cancer etc, it is important to quantify the regional deposition, especially in the distal alveolated region to predict therapeutic efficacy. Thus accurate models of regional deposition in the lung are necessary both from clinical and scientific points of view to target specific regions of the lung with greater accuracy (Manshadi *et al.*, 2019; Dames *et al.*, 2007).

This work is focused on investigating the parametric effects on aerosol deposition in straight micro-capillaries as well as to develop validated model. The literature pertaining to aerosol deposition in circular pipes is quite mature, but at the same time mostly focused on high Re turbulent flows or laminar flows ($Re \sim 10^1 - 10^2$). Through an ex-

perimental study, [Kim *et al.* \(1984\)](#) showed that the aerosol deposition in a straight pipe increases with increasing particle size. However their study is restricted to $\sim 0.5\text{cm}$ tubes with the corresponding Re ranging from 140 to 2800. Similarly, the studies of [Montgomery and Corn \(1970\)](#); [Malet *et al.* \(2000\)](#); [Muyschondt *et al.* \(1996\)](#); [Friedlander and Johnstone \(1957\)](#) with higher diameter pipes is associated with very high $Re \sim 10^5$ that addresses deposition in high Re turbulent flows and fails to explain deposition in lung airways. The experiments done by [Sehmel \(1968\)](#) were also in the range of $Re \sim \mathcal{O}(10^4)$. In all the cases, the deposition was characterized in a range of Re where impaction dominates the deposition process. The lacuna that the current work attempts to fill is to span a wider a range of Re to gain a holistic understanding of aerosol deposition of all the underlying physical processes. The overarching goal is to construct a model that will be able to predict deposition in the entire lung based on extensive measurements of aerosol deposition in phantom bronchioles spanning five order of magnitude of Reynolds numbers. The study also points to a minimal set of dimensionless variables that are sufficient to capture the deposition efficiency over wide range of Re ($10^{-2} \leq Re \leq 10^3$) that defines the novelty of this work.

CHAPTER 3

Experimental Methods

This chapter highlights the experimental setup and the procedure of collecting and analysing deposition samples in details. The experiments are carried out with capillaries of varying diameters ($0.3mm - 2mm$) mimicking 7^{th} to 23^{rd} generation of human lungs. The experimental Re ranges from Re ($10^{-2} \leq Re \leq 10^3$) that mimics the flow conditions of the entire lungs for a single breath.

3.1 Experimental setup

The experimental setup shown in Figure 3.1 consists of a horizontal micro-tubule (phantom bronchiole) which is attached to a syringe. Different diameters and lengths of these tubules are intended to mimic different generations of bronchioles in the lung as indicated in Table 3.1. Polytetrafluoroethylene (PTFE) tubules of different diameters:

Table 3.1: A table listing bronchiole diameter as a function of the branching generation in the lung. Typical Re is calculated based on tidal volume of $500ml$ and a $4s$ breathing cycle.

Typical bronchiole dia (mm)	Lung generation	Typical Re
10	0 \rightarrow 6	$10^3 - 10^2$
1.5	7 \rightarrow 10	40
1	11 \rightarrow 13	5
0.5	14 \rightarrow 21	$10^{-1} - 10^{-2}$
0.3	22 \rightarrow 23	7×10^{-3}

$0.3mm$, $0.5mm$, $1mm$, $1.5mm$ and $2mm$ and with good surface finish are purchased from Cole-Parmer[®], were used as phantom bronchioles. These tubules were translucent, chemically inert, have low water absorption property $< 0.01\%$ and have very low coefficients of friction ($\sim 0.05 - 0.1$) which is third lowest of any solid. The non-sticky nature of this material helps in complete removal of the deposited aerosol by washing with water.

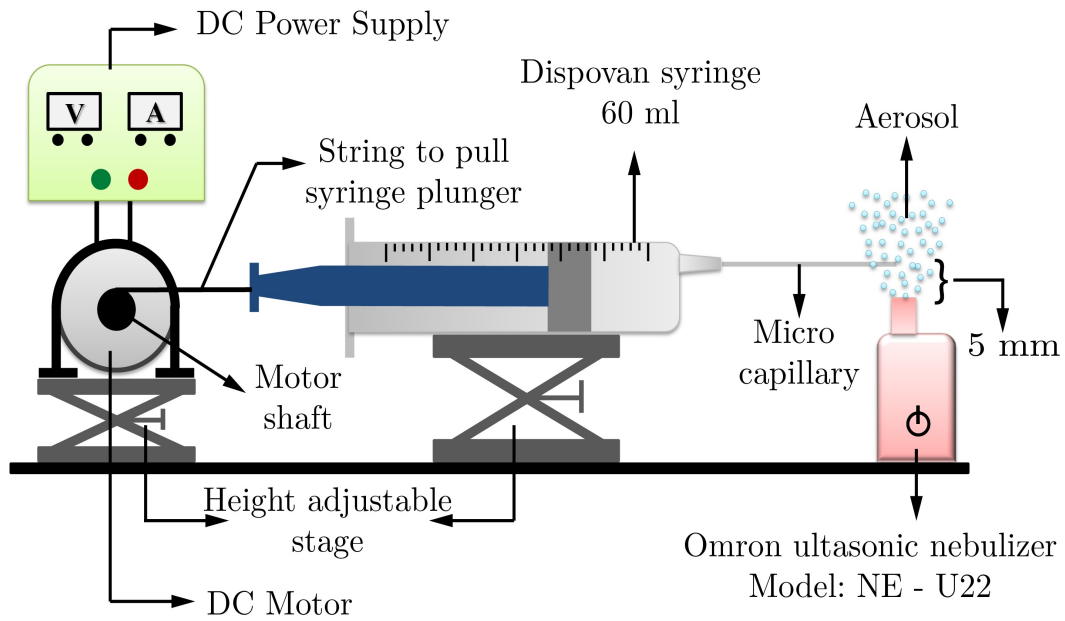


Figure 3.1: Schematic of the experimental setup consisting of aerosol generator, micro-capillary (phantom bronchiole), syringe with a motor arrangement to draw the plunger at a constant velocity. The inlet of the bronchiole is placed at a height of 5mm above the geometric center of the nebulizer exit. Different flow conditions through the micro-capillaries were achieved by controlling the rotational speed of the 12V DC motor using a 32V , 2A DC power supply.

A syringe plunger intended to drive the flow is connected to the shaft of a DC motor. A DC motor of ratings 10rpm at 12V and 30rpm at 12V is used to achieve different suction rates. The flow rates has been verified several times before experiment by tracing the location of plunger within stipulated time. With the rotation of the motor shaft, the plunger is actuated at a constant rate to draw the aerosol exiting the nebulizer into the PTFE tubule. The rotational speed of the motor is varied to obtain different flow rates. The rotational speed is in turn, varied by varying the voltage at the motor terminals with the help of a 32V , 2A , DC power supply. For very low suction rates ($Re \ll 1$), a syringe pump is used. Interestingly, the lowest Re experiment involved an ultra low flow rate which required that a single experiment be performed over a duration of 5hours for reliable measurements. An ultrasonic mesh type nebulizer (Omron Model: NE-U22) is used to generate a finely atomized, gently rising aerosol plume. The setup is mounted on a height adjustable stage to ensure proper motion of the plunger and to maintain the micro-tubule at a height of 5mm from the nebulizer exit, where all drop size measurements were performed.

3.2 Preparation of aerosol liquid

The aerosol liquid composed of water as the fluid medium and was loaded with boron quantum dots (Reed *et al.*, 1989), which acted as fluorophores. The photo-physical properties of quantum dots, including carbon quantum dots (CDs), depend on their size (Song *et al.*, 2016) as its band gap originates from quantum confinement. The tuning of band gap, which is measured by quantum yield (QY), can be achieved by incorporating trap sites while introducing functional groups during the synthesis of CDs. In order to increase QY, trap sites of CDs are often doped with hetero atoms such as nitrogen (Mi *et al.*, 2013), boron (Fan *et al.*, 2013) or phosphorous (Ananthanarayanan *et al.*, 2014) depending on the application.

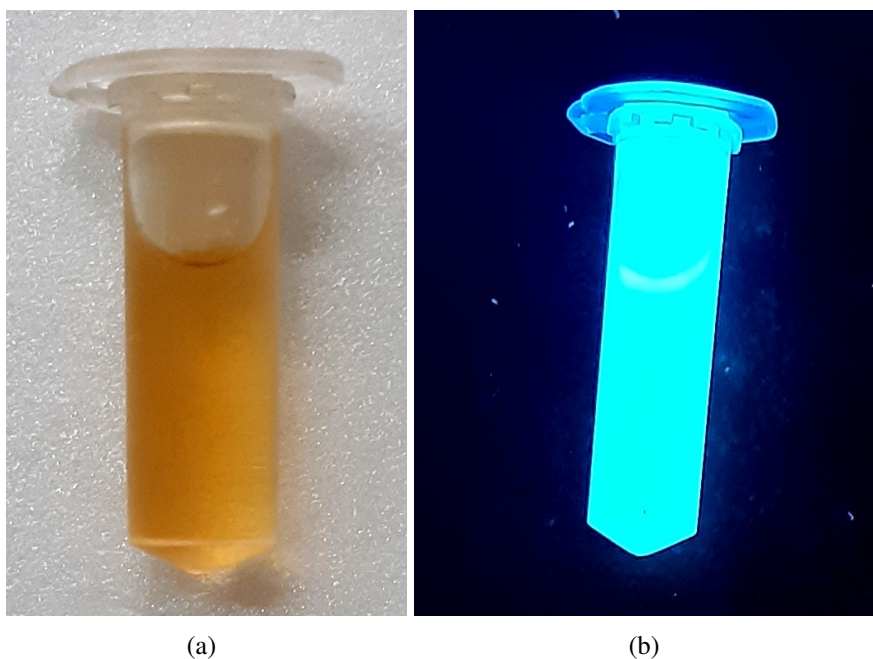
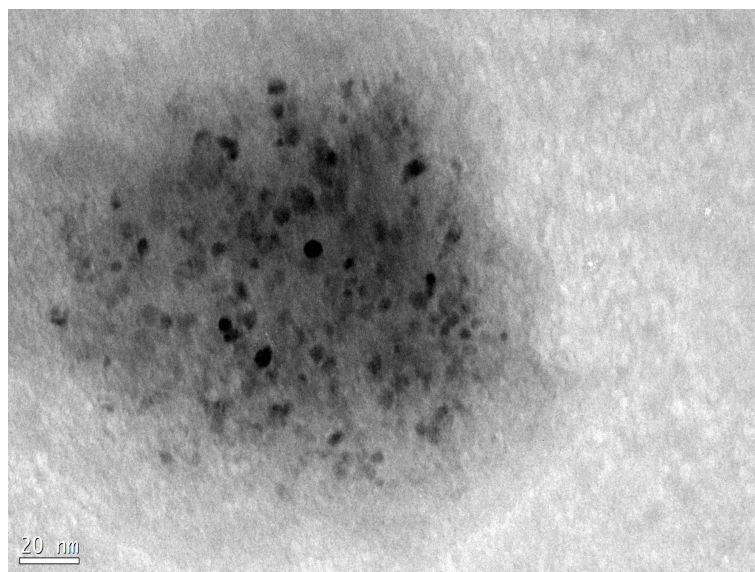
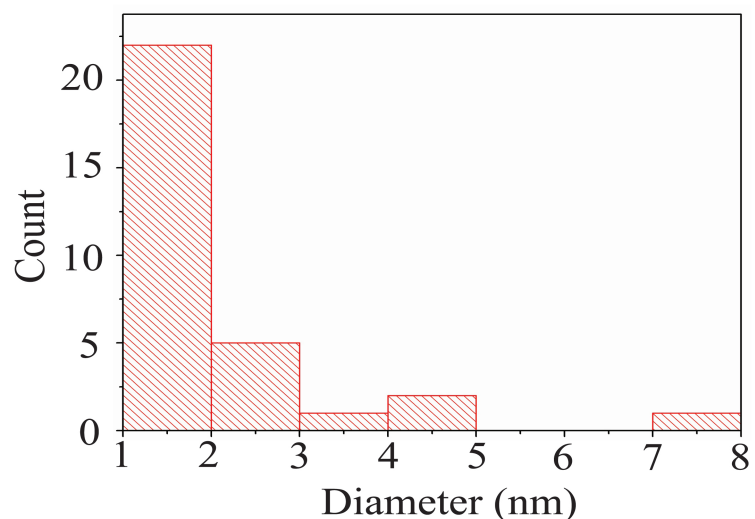


Figure 3.2: Images of vials (a) containing a solution with freshly prepared Boron doped Carbon Dots (BCD) and (b) showing emission of blue light by BCD when excited by ultraviolet light of wavelength $350nm$.

The synthesis of Boron doped Carbon Quantum Dots (BCDs) was done in the laboratory through a bottom up-process. Care was taken to ensure that the Deionised (DI) water used for synthesis of CDs and BCDs has a pH of 7. All the chemicals used for synthesis were sourced from Sigma-Aldrich[®], Merck[®], Fischer-Scientific[®] and Spectrochem[®]. Equimolar concentration solutions at $0.5M$ each of boric acid (Boron precursor) and glucose (carbon precursor) were prepared with $10ml$ of DI water and mixed using a magnetic stirrer at $300rpm$ for 15 minutes. The solution was transferred



(a)



(b)

Figure 3.3: (a) Transmission Electron Microscopy (TEM) image of Boron doped Carbon Quantum Dots. Scale is indicated as a white bar. (b) Histogram of the size distribution of BCD estimated from the TEM images. The BCD distribution is nearly mono-disperse.

to a glass bowl and treated under commercial microwave (IFB) radiation of 700W for 5min. The resulting solid was then dried in vacuum to remove all volatiles and dispersed in 500ml of DI water to form an olive green solution as shown in Figure 3.2(a). The larger particles were sorted out by centrifugation at 1500g for 15min and filtered in vacuum using a 10kDa filter. The resultant solution emits blue light when excited by a wavelength of 350nm as shown in Figure 3.2(b). The morphological characteristics of BCDs were investigated by Transmission Electron Microscopy (TEM) (see Figure

3.3(b) for a representative image). Their size distribution was estimated from the TEM images with the help of ImageJ[®]. Figure 3.3(b) shows the obtained size distribution. As can be seen, the BCDs are nearly mono-disperse and range in size from $1nm$ to $2nm$ (Figure 3.3b) which is approximately 5 orders smaller than the smallest dimension of the tubule used in the experiment. Since the BCDs were nearly mono-disperse, the emitted fluorescence spectrum is likely to be in a narrow wavelength band.

3.3 Generation and characterization of aerosol plume

There are several methods of droplet generation from a bulk liquid according to the existing literature. The disintegration of bulk liquid requires external forces that contribute in overcoming the surface energy and provide kinetic energy to the droplets. The generation of droplets using pressure swirl or air-blast atomizers and shear break up of jets by air is common in different industrial applications. The use of ultrasonic mesh and compressed air for atomization is common in fogger, humidifier and drug nebulizers. In case of conventional atomizers and breakup of jet in cross flow (JICF) the breakup processes under goes ligament formation, primary atomization and secondary atomization (Mallik *et al.*, 2020). The ligament formation zone consists of big blobs of liquids disintegrated from the bulk liquid, which further breakup to form droplets. This is called primary atomization. The primarily atomized drop undergoes further breakup to form smaller droplets that are stable due to higher surface energy. This different stages of breakup for conventional atomizers and JICF gives rise to a wide range of droplet sizes. On the contrary the ultrasonic or compressed air atomization do not under goes different stages of breakup which results in generation of mono dispersed drops. The figure 3.4 shows a comparative study of droplet size distribution using different atomization process. The size distribution of Omron[®] make jet and ultrasonic mesh nebulizer, JICF (Mallik *et al.*, 2020) and solid cone spray (Make: Delevan[®]) is estimated using Phase Doppler Particle Analyzer (PDPA). It is evident from the figure that nebulizers produces mono dispersed drops of smaller sizes in comparison to the other conventional atomization techniques.

In this study, a mesh type ultrasonic nebulizer was used to generate the aerosol plume at a constant rate of $0.25ml/min$. The droplet size and velocity distributions

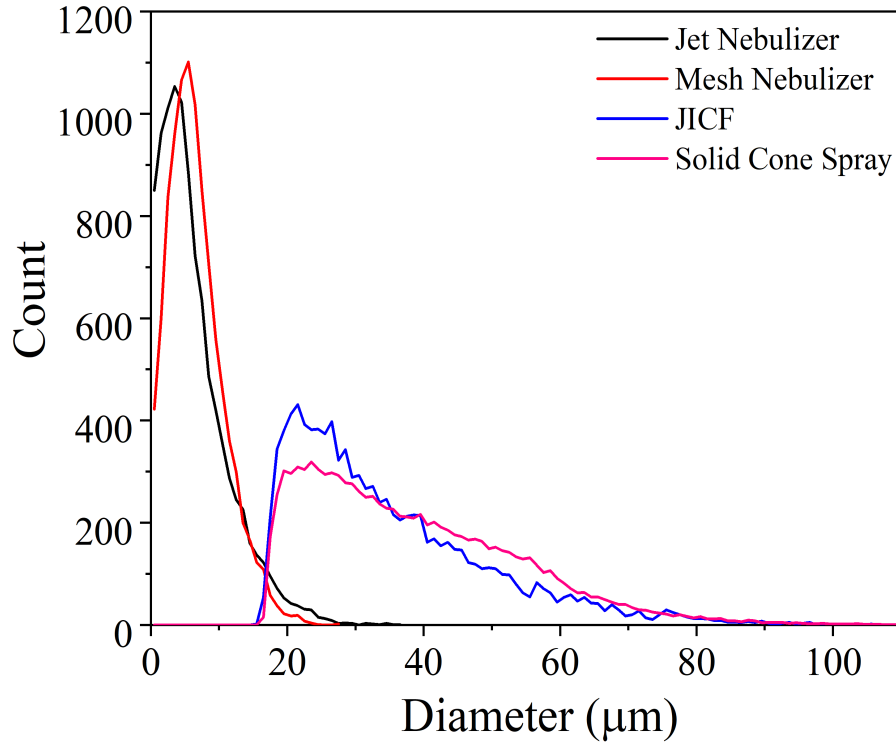


Figure 3.4: Plot of droplet size distribution for Omron® make jet nebulizer, mesh nebulizer, JICF (Mallik *et al.*, 2020) and solid cone spray (Make: Delevan®). In the figure it is evident that the size distribution of the spray and JICF spans a wide range of diameters where as the distribution of the nebulizers is comparatively mono dispersed.

of the aerosol plume generated by the nebulizer were characterized using a TSI® make PDPA. It is a non-intrusive, laser-based, single particle and point measurement system which works on the principle of interferometric particle sizing. The optical settings employed for the PDPA are given in the table 3.2. Since accurate size measurement depends on phase difference of photo detectors, phase calibration was periodically performed to avoid unexpected phase delay. The optical settings of the PDPA were adjusted such that the particle diameter measurement range is $0.5\mu m$ to $165\mu m$ with an estimated accuracy of $\pm 0.1\mu m$ over the entire range. A wide range of velocity measurements from $-100m/sec$ to $200m/sec$ was also possible through the appropriate band pass filter choice. As a result, drop size and velocity were measured with an accuracy of $\pm 0.2\%$. Finally, the photo multiplier tube (PMT) voltage is chosen such that it does not add noise to the data while producing a good data rate.

The diameter and velocity of the aerosol exiting the nebulizer is measured at different radial locations, $2mm$ apart, at an axial distance of $5mm$ from the nebulizer exit as shown in figure 3.5. For ensuring high statistical reliability of the PDPA measurement,

Table 3.2: Optical settings of PDPA

Optical settings	Values
Transmitter Wavelength	532nm
Transmitter Focal Length	363mm
Laser Beam Separation	50mm
Laser Beam Diameter	2.10mm
Beam Expander Ratio	1
Beam Waist	117.09 μ m
Fringe Spacing	3.8715 μ m
Bragg Cell Frequency	40MHz
Off - axis angle	43°
Mode of scattering	Refraction
Refraction index	1.33

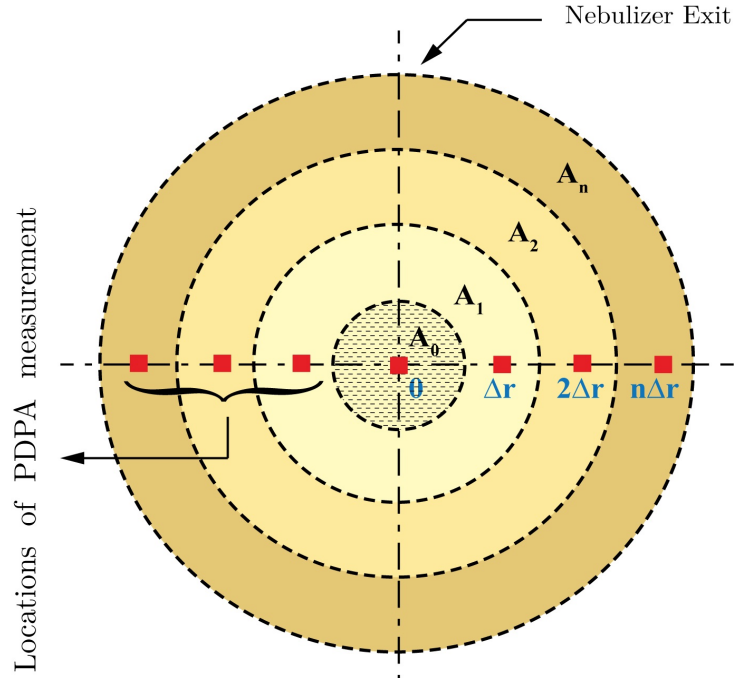
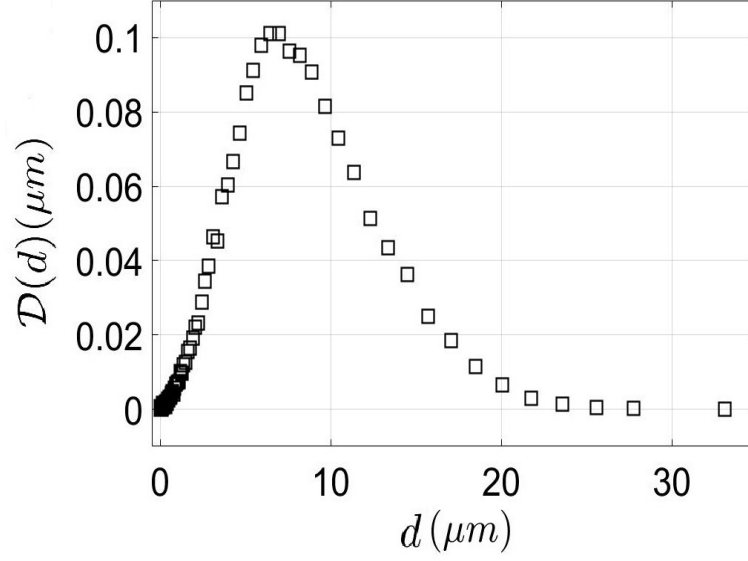


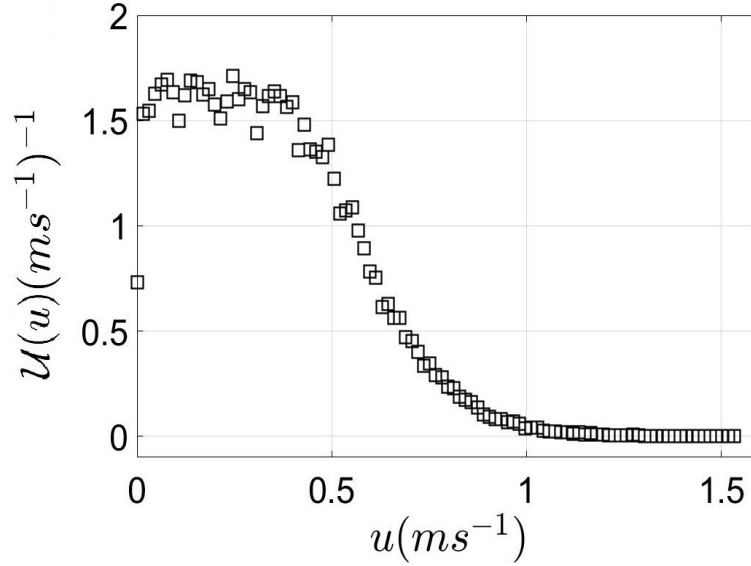
Figure 3.5: Schematic of measurement location of drop size and velocity, 5mm above the nebulizer exit, using Phase Doppler Particle Analyzer

10000 drops were sampled at each measurement location. PDPA only yields point-wise drop size distribution data. A global size and velocity distribution, characteristic of the entire nebulizer was calculated from the point-wise data following the method of Tratnig et al. [Tratnig and Brenn \(2010\)](#) and Dhivyaraja et al. [Dhivyaraja et al. \(2019\)](#). The global diameter *pdf*, $\mathcal{D}(d)$ and velocity p.d.f, $\mathcal{U}(u)$ is given by:

$$\mathcal{D}(d) = \frac{\sum_1^j \dot{n}(r_j, D_i) 2\pi r_j \Delta r}{\sum_1^j \sum_1^i \dot{n}(r_j, D_i) 2\pi r_j \Delta r}, \quad (3.1)$$



(a)



(b)

Figure 3.6: Plot of (a) the global diameter probability distribution function and (b) the global velocity probability distribution function, both measured using PDPA. The most probable drop size of size $6.5\mu m$. Most drops were moving at a velocity less than $0.5m s^{-1}$ indicating that the aerosol plume was finely atomized and gently rising, as desired.

$$\mathcal{U}(u) = \frac{\sum_1^j \dot{n}(r_j, u_i) 2\pi r_j \Delta r}{\sum_1^j \sum_1^i \dot{n}(u_j, D_i) 2\pi r_j \Delta r}. \quad (3.2)$$

Here, D_i is the aerosol size and u_i is the axial component of the aerosol velocity and g is calculated based on number flux density of the drops for diameter and velocity given by $\dot{n}(r_j, D_j)$ and $\dot{n}(r_j, u_j)$ respectively. The global probability density functions

of both drop size and velocity are true representations of nebulizer performance since they are insensitive to external factors. The global aerosol drop size *pdf* ($\mathcal{D}(d)$) is shown in Figure 3.6(a). It shows a maximum probability for $6.5\mu m$ drops which is taken as the characteristic droplet size in the aerosol plume. The velocity *pdf* ($\mathcal{U}(u)$) in figure 3.6(b) denotes the most probable velocity occurs for $0 < u(m/s) < 0.5$. The mean velocity from this *pdf* was found to be $0.44m/s$. From these measurements one can conclude that a finely atomized, gently rising aerosol plume was formed by the nebulizer.

The deposition fraction is measured in each experiment as the ratio of the deposited aerosol to the amount of aerosol that is present in the volume of air drawn in to the bronchiole. The aerosol volume fraction (α_0) from the nebulizer at a point is estimated directly from the PDPA measurements. The figure 3.7 shows that the concentration (α_0) of mesh nebulizer is least, 6.2×10^{-5} , among the other atomizers. Since the α_0 is $\sim \mathcal{O}(10^{-5})$, the aerosol plume can be construed to be extremely dilute and consisting of non-interacting droplets.

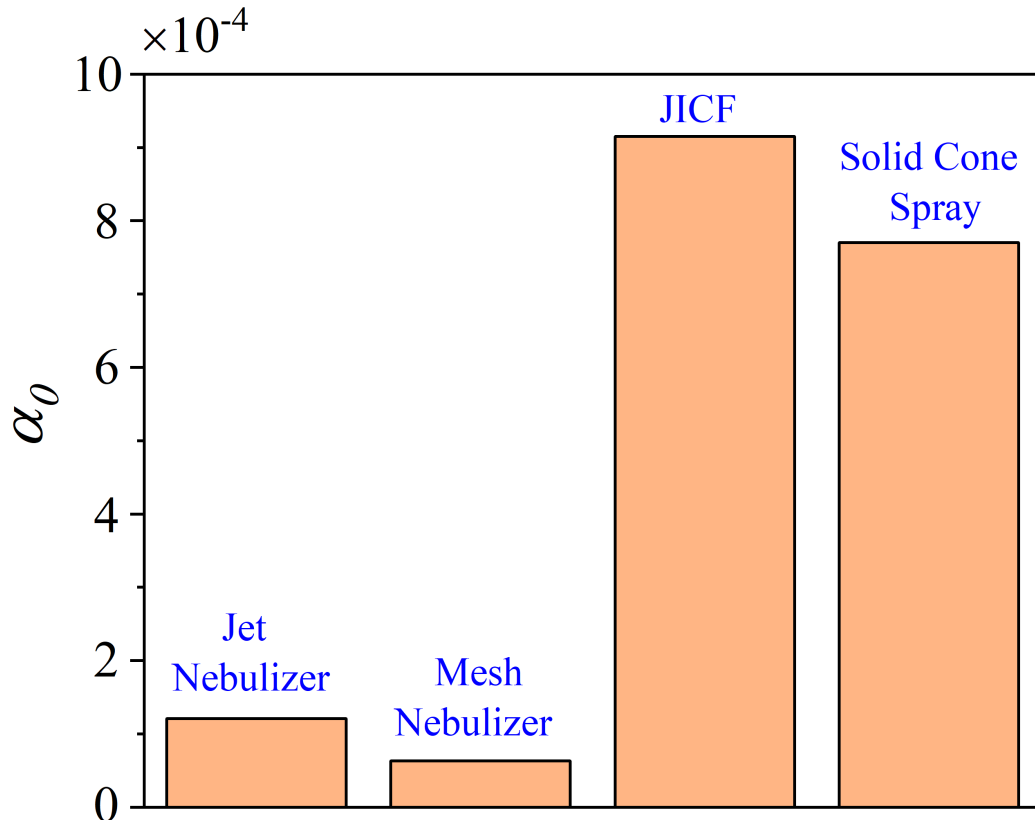


Figure 3.7: Bar plot showing concentration (α_0) of the generated drop for jet nebulizer, mesh nebulizer, JICF and solid cone spray. Among all, mesh nebulizer is found to have lowest droplet concentration of 6.26×10^{-5} that confirms the aerosol plume to be dilute and non - interacting.

3.4 Preparation and analysis of deposition samples

The fluorescence signal from the BCDs in the sample was measured using a Horiba FluoroMax[®] spectrofluorometer. The instrument consists of a 150W Xenon arc lamp, which were self-calibrated for all wavelength drives and slits. The fluorescence detector consisted of a Photo Multiplier Tube (PMT) which can capture emission wavelengths from 185nm to 850nm with an accuracy of $\pm 0.5nm$ and a repeatability of 0.1nm. The water Raman signal to noise ratio was found to be 6000 : 1, as calculated by the First Standard Deviation (FSD) method, and 16000 : 1, as calculated by Root Mean Square (RMS) method. This ensured that the fluorescence signal from the BCDs was not confounded by signal from other sources.

The experiment involved an aerosol plume flowing through the PTFE micro-capillaries at a prescribed flow rate. The deposited aerosols within the capillary were then flushed thoroughly with 5ml of DI water to prepare the samples for measuring aerosol concentration. From this, a sample volume of 2ml of the solution is taken in the cuvette and excited with the wavelength of 340nm with a slit width of 3nm. The emission intensity was recorded for different wavelengths varying from 405 to 610nm, with a slit width of 5nm. The sensitivity of the instrument was checked for an empty cuvette, a cuvette containing DI water as well as for a cuvette containing fluorescence samples for the lowest deposition recorded. It was found that the intensity of the water containing fluorescence sample is at least one order higher than that for normal DI water. The intensity obtained for various aerosol deposition measurements is compared with the intensity obtained from 1ml of aerosol liquid (i.e. BCD) dissolved in the same volume of DI water used for flushing the capillaries. This is taken as the reference value for estimating the deposition in the tubule. Finally, the concentration of the deposited aerosol was calculated from the fluorescence measurement.

CHAPTER 4

Results and Discussion

This chapter describes the results obtained from the experimental study of aerosol deposition in phantom distal bronchioles. The first part of this chapter introduces the deposition parameters considered in the experiment and their dimensionless forms. The latter part contains an in-depth discussion of the obtained results, describing the effect of individual parameters on deposition.

4.1 Experimental Parameters

The deposition of nebulized particles of mean diameter $6.5\mu m$ is investigated for microcapillaries of differing lengths and diameters to mimic different generation bronchioles. The aerosol properties such as kinematic viscosity, droplet size, concentration etc. (Feron, 1994) and the tubules dimensions greatly affects the deposition. The deposition concentration of aerosol in these phantom bronchioles can be expressed as a function of several parameters as

$$d = f(L, D, Q, T, \nu, D_{10}, \alpha_0). \quad (4.1)$$

Here,

d = the measured aerosol deposition (ml),

L = the length of bronchiole (mm),

D = the bronchiole diameter (mm),

Q = the volume flow rate (ml/s),

T = the time duration of the flow (s),

ν = the kinematic viscosity of air (m^2/s),

D_{10} = the mean droplet diameter (μm).

α_0 = is the volume fraction of aerosol from nebulizer (ml of aerosol per ml of space),

From a careful dimensionless analysis, one can identify the following relevant dimensionless parameters from the above parameters. These dimensionless parameters are defined in Table 4.1.

Table 4.1: Definition of dimensionless parameters

Dimensionless parameter	Definition
Deposition fraction (D_F)	$d/(\alpha_0 QT)$
Aspect Ratio (\bar{L})	L/D
Dimensionless bronchiole diameter (\bar{D})	D/D_{10}
Reynolds number (Re)	$4Q/(\pi\nu D)$
Dimensionless Time (\bar{T})	$4QT/(\pi D^3)$

Aerosol deposition has been investigated for a wide range of flow conditions, $10^{-2} \leq Re \leq 10^3$, mimicking the flow in different generation bronchi and bronchioles. The total volume of air that has passed through the bronchiole during the experiment is QT , which is the flow rate multiplied by the breathing time. As a result the total volume of aerosol that entered the bronchiole is $\alpha_0 QT$. The deposition fraction (D_F) defined as the fraction of the exposed aerosol ($\alpha_0 QT$) that has been deposited in the bronchiole, is likely to increase with increasing length of the bronchiole and time of exposure (Asgharian *et al.*, 2004; Koullapis *et al.*, 2020; Khajeh-Hosseini-Dalasm and Longest, 2015). Thus to normalize for these effects, a dimensionless deposition fraction per unit (dimensionless) length and (dimensionless) time, δ is defined as

$$\delta = \frac{D_F}{\bar{L}\bar{T}} \quad (4.2)$$

Equation 4.1 can be rewritten in terms of the dimensionless parameters in Table 4.1 as

$$\delta = G(Re, \bar{D}, \bar{L}, \bar{T}, \alpha_0) \quad (4.3)$$

It is an endeavour of this work to identify a physics-consistent and universal function G as in equation 4.3 from experimental data.

The experiments are repeated several times (minimum 5 times, in few cases 8 - 10 times) for different Re and aspect ratio to ascertain repeatability of deposition fraction in the phantom bronchioles. The maximum estimated uncertainty for all the measured parameters was within $\pm 5\%$ calculated based on (Kline, 1953; Moffat, 1988) formula

as given in equation 4.4.

$$\omega_R = \left[\left(\frac{\partial R}{\partial x_1} \omega_1 \right)^2 + \left(\frac{\partial R}{\partial x_2} \omega_2 \right)^2 + \dots + \left(\frac{\partial R}{\partial x_n} \omega_n \right)^2 \right]^{\frac{1}{2}} \quad (4.4)$$

Here ω_R is the uncertainty in the result and $\omega_1, \omega_2, \dots, \omega_n$ are uncertainties in the measurement of independent variables. R is given by $R = R(x_1, x_2, x_3, \dots, x_n)$ where x_1, x_2, \dots, x_n are the independent variables. The values are given in the table 4.2. The effect of the various dimensionless groups on the dimensionless deposition, D_F and δ are discussed in the later section.

Table 4.2: Uncertainty in the measured and calculated parameters.

Derived parameters	Estimated uncertainty
Deposition fraction (D_F)	$\pm 5\%$
Aspect Ratio (\bar{L})	$\pm 1\%$
Dimensionless diameter (\bar{D})	$\pm 1.5\%$
Reynolds number (Re)	$\pm 0.2\%$
Dimensionless Time (\bar{T})	$\pm 0.6\%$
δ	$\pm 5\%$

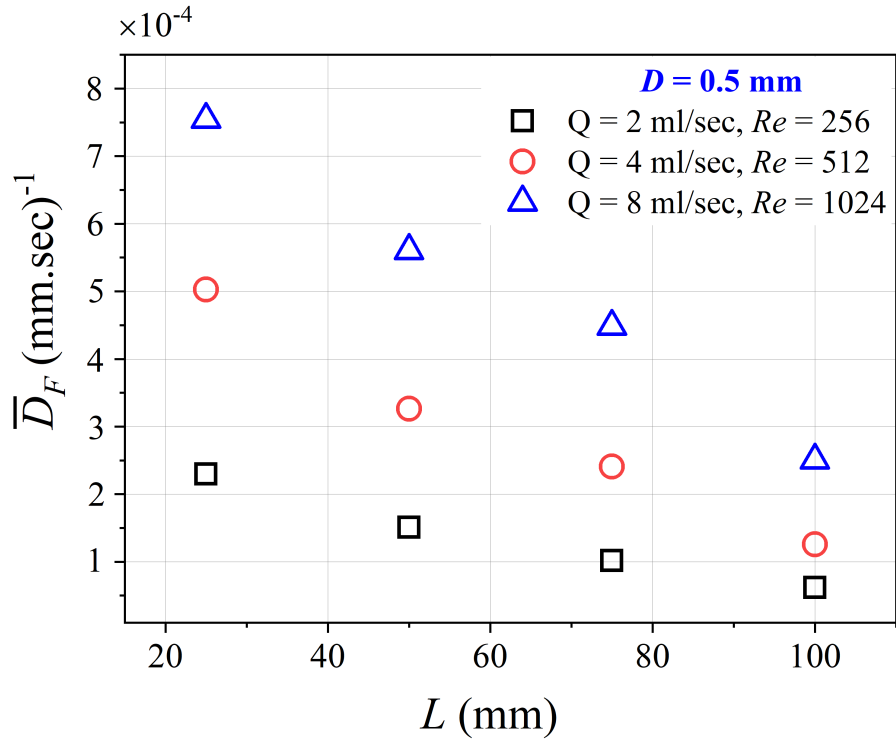
4.2 Effect of \bar{L} , \bar{D} and Re on deposition

The length of the capillary directly influences the aerosol deposition since it determines the aerosol travel time within the capillary. Figure 4.1a shows that the D_F per unit length per unit time is higher for small capillaries and it decreases as the capillary grow longer. Figure 4.1 (b) presents the variation of δ with \bar{L} for different values of Re . The dimensional form of this variation is shown in figure 4.1 (a), where δ is replaced by deposition fraction (D_F) per unit length of the capillary, per unit time represented by \bar{D}_F . Within the lung, every bronchus is dichotomously branched into two bronchi at each generation. Thus the flow rate gets halved, which causes the Re to become half of the previous value at every generation. The Re is chosen such that it spans the range of Reynolds numbers encountered in the upper bronchi, where inertial effects are significant. \bar{D} was maintained constant at 77, which denotes the capillary diameter to be 0.5mm. The results show that δ decreases with an increase in \bar{L} . In other words, the deposition per unit length and unit time decreases as the length of the bronchiole increases (Ref: Figure 4.1(a)). This shows the inverse relation of δ with \bar{L} for all Re .

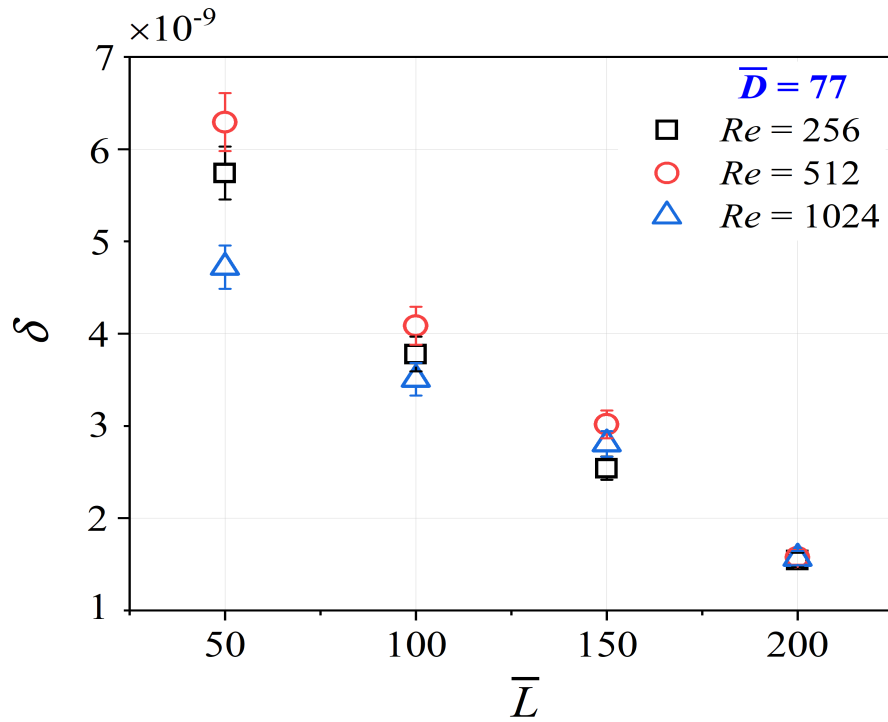
For small aspect ratio, \bar{L} , the effect of Re is visible. This is due to the fact that for small \bar{L} , inertial effects play a role in decreasing deposition. However, for high aspect ratios, the effect of Re is insignificant.

The effect of particle size on regional deposition has been studied in the past literature (Lippmann and Albert, 1969; Mitchell *et al.*, 1987; Glover *et al.*, 2008; Malvè *et al.*, 2020) but the effect of bronchiole diameter on aerosol deposition is least studied. With different generations of the lungs the bronchiole diameter varies continuously and affects deposition. The effect of \bar{D}_F for different capillary diameter ranging from $0.3\text{mm} - 2\text{mm}$ is shown in figure 4.2 (a), for constant $Re = 512$. The diameter of the tubules mimics 7^{th} to 23^{rd} generations of the lungs. The effect of dimensionless bronchiole diameter on deposition (δ) is shown in Figure 4.2 (b) for various aspect ratios (\bar{L}), maintaining Re constant. δ , representing deposition fraction per unit length of the bronchiole per unit suction time, increases with an increase in bronchiole diameter, represented by \bar{D} . The rate of increase of δ decreases for $\bar{D} > 150$. This is because for a constant Re , an increase in bronchiole diameter causes the flow rate to increase which results in higher deposition. The value of δ is lowest for $\bar{L} = 200$ and increases with decrease in \bar{L} similar to the trends in figure 4.3 (b).

The particle deposition in lungs greatly depends on the airflow rate (Zhang *et al.*, 2000; Koullapis and Kassinos, 2018). Although airflow rate can be represented non dimensionally by flow Re but Re changes with diameter even if the flow rate is constant. In a real case scenario, each generations of lung may undergo different air flow rates based on different breathing conditions (Deng *et al.*, 2019a). Figure 4.3 (a) shows the plot of \bar{D}_F for variable tubule diameter and air flow rates. The aspect ratio is kept constant, $\bar{L} = 100$. At each lung generation the airways gets bifurcated causing the flow rate to be halved. Thus in the experiment the flow rates increases twice the previous value. Figure 4.3 (b) is the plot of δ versus \bar{D} for different flow conditions. The suction flow rates are represented non-dimensionally by a particle-based Reynolds number $Re_p = 4Q/(\pi\nu D_{10})$. Interestingly, $Re_p = Re\bar{D}$, which can be understood as a Reynolds number based on the mean particle size, D_{10} . As can be seen, δ increases with an increase in the dimensionless bronchiole diameter (\bar{D}), but is not dependent on the particle based Reynolds number. This is unlike the data presented for a constant Re in Figure 4.2 (b). As \bar{D} increases at a constant $Re\bar{D}$, the mean velocity of the air flow in the bronchiole decreases. This causes the rate of deposition to increase, since

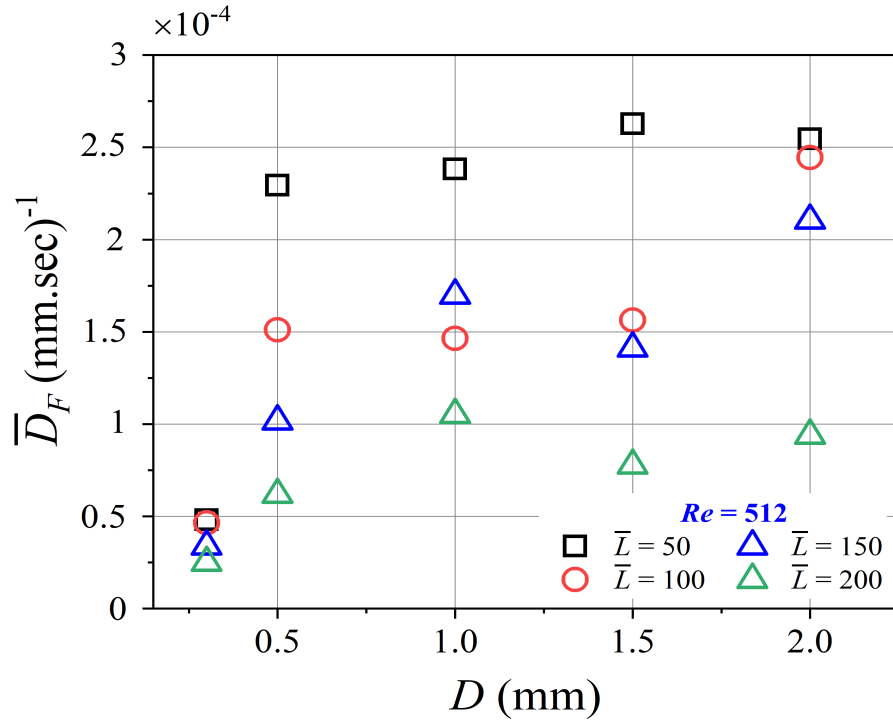


(a)

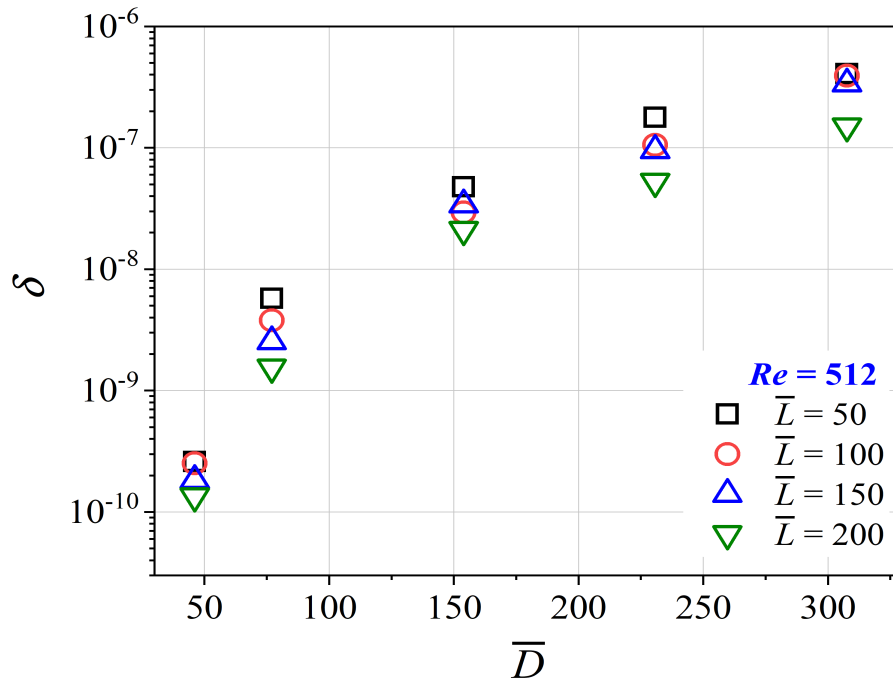


(b)

Figure 4.1: Plot of (a) variation of deposition fraction per unit capillary length per unit time (\bar{D}_F) with capillary length (L) and (b) the variation of dimensionless deposition (δ) versus aspect ratio (\bar{L}), for different Reynolds number (Re). The data shows an inverse relation of δ with bronchiole aspect ratio (\bar{L}). For high \bar{L} , the effect of Re is negligible.



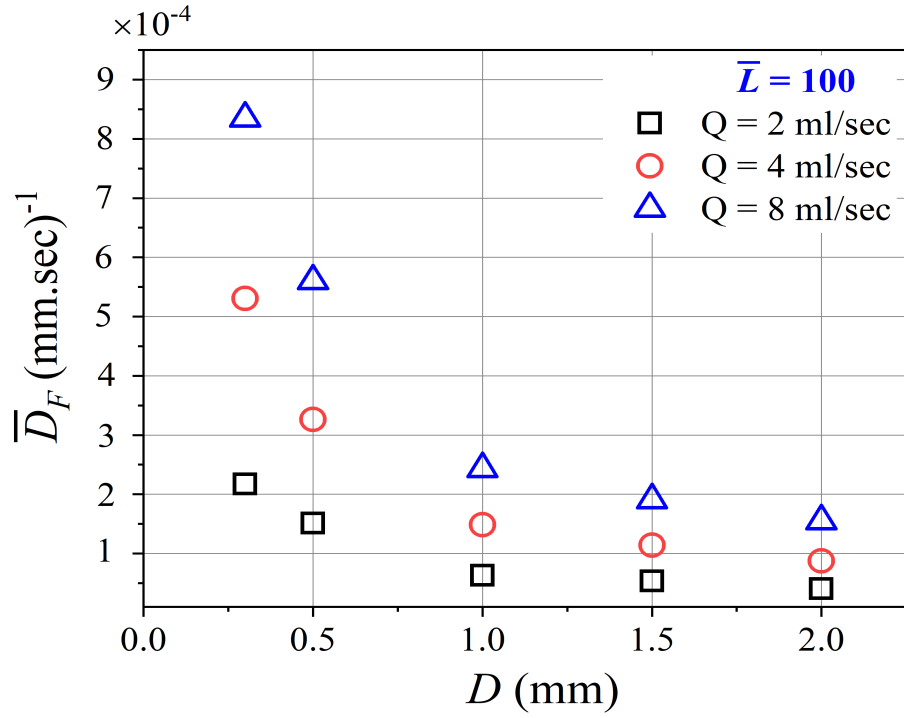
(a)



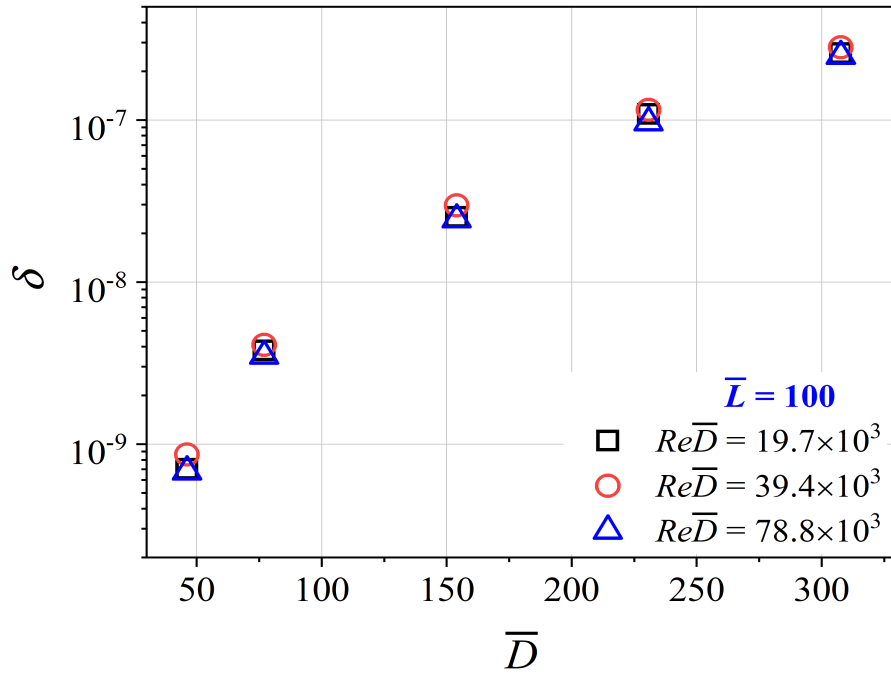
(b)

Figure 4.2: Plot of (a) deposition fraction per unit capillary length and unit time (\bar{D}_F) with tubules diameter (D) and (b) dimensionless deposition (δ) versus dimensionless bronchiole diameter (\bar{D}), for varying bronchiole aspect ratio (\bar{L}). Reynolds number was constant at $Re = 512$. The tubules diameter mimics 7th – 23rd generation of the lungs. It is seen that with increase in \bar{D} the dimensionless deposition (δ) increases, while \bar{L} still follows the inverse relation with δ for a constant \bar{D} .

diffusion-driven and gravitational settling become relevant. It is important to note that both Figures 4.2 (b) and 4.3 (b) are plotted with the δ co-ordinate being plotted on a logarithmic axes. A factor of 6 change in \bar{D} brings about three orders of magnitude change to the deposition fraction. Therefore, it can be concluded that the bronchiole diameter is an important parameter in determining aerosol deposition.



(a)



(b)

Figure 4.3: Plot of (a) deposition fraction per unit capillary length and unit time (\bar{D}_F) with tubules diameter (D) and (b) dimensionless deposition (δ) versus \bar{D} for varying particle-based Reynolds number ($Re\bar{D}$), keeping aspect ratio $\bar{L} = 100$. It is seen that δ increases with \bar{D} . $Re\bar{D}$ does not affect the deposition.

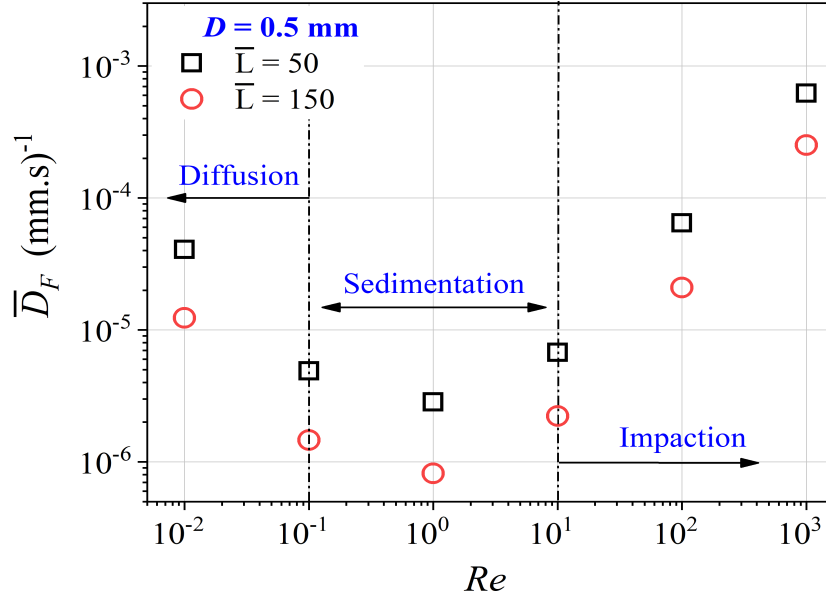
4.3 Deposition for the entire lung-specific Re range

The tidal volume of a healthy adult human lung is approximately $500ml$ or $7kg$ / body mass per inspiration (Ricard, 2003; Mackay *et al.*, 2020). The tidal volume is described as the volume of air delivered to the lung with each breath when no extra effort is applied. Considering the flow of the air to be $500ml$ for a breathing cycle of 4 seconds (i.e. 2 seconds each for inspiration and expiration) (Fox, 2015), the Reynolds number (Re) in trachea ($G = 0$) and alveoli ($G = 23$) are respectively, on the $\mathcal{O}(10^3)$ and $\mathcal{O}(10^{-2})$ (Ref: Figure 1.3). This huge variation of Re within different generations of the lung is responsible for different modes of aerosol deposition in different regions, such as, deposition by impaction, sedimentation and diffusion (Grotberg, 2011; Rostami, 2009; Cheng, 2014; Svartengren *et al.*, 1987).

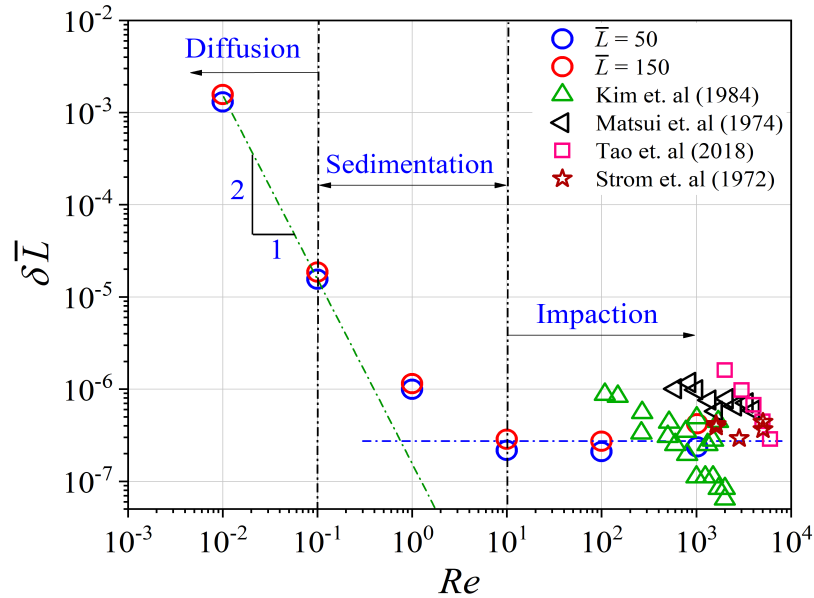
In this study the experiments were carried out for different orders of Re ranging from $10^{-2} \leq Re \leq 10^3$, representing the entire lungs. The existing literature speaks about the total deposition in lungs, numerically (Kolanjiyil and Kleinstreuer, 2016; Kolanjiyil *et al.*, 2017; Kolanjiyil and Kleinstreuer, 2017; Brand *et al.*, 2000; Jaques and Kim, 2000; Madureira *et al.*, 2020; Dolovich, 2001). To the best of our knowledge, this is the first report where the entire dynamic range of lung-relevant Reynolds numbers have been explored in one experiment. Figure 4.4 (a) represents the plot of \bar{D}_F for entire range of Re , that happens in human lungs in a single breath. A minimum in D_F can be observed nearly at $Re = 1$, where the velocity is in $\sim \mathcal{O}(10^{-1})$ m/s and gravitational deposition dominates over inertial deposition. For impaction dominated zone (i.e. $10 \leq Re \leq 10^3$) and in diffusion dominated zone ($10^{-2} \leq Re \leq 1$), D_F takes on higher values. This is because a high suction rate carries greater number of aerosol particles that impact and deposit on the bronchiole walls. In the diffusion-dominated zone again, D_F increases with a decrease in Re . This is possibly due to the fact as Re decreases, thermal fluctuations become dominant in moving the aerosol towards bronchiole walls. Thus for a sufficiently long exposure time, the aerosol diffuses inside the bronchiole causing increased deposition.

The effect of Re on $\delta\bar{L}$ is investigated for $\bar{L} = 50$ and 150 in Figure 4.4 (b). The experiment has been carried out for two aspect ratios, to verify the inverse relation between δ and \bar{L} still follows at low Re condition. It may be recalled that $\delta\bar{L}$ is the

dimensionless rate of deposition. It can be seen that when $\delta\bar{L}$ is plotted against Re , the data in Figure 4.4 (b) nicely collapse onto a single curve. This data collapse points to a minimal set of dimensionless parameters that is required to completely describe aerosol deposition. Two asymptotic regimes can be seen in Figure 4.4 (b). For $Re > 1$, $\delta\bar{L}$ is independent of Re . This is the parametric regime where deposition happens mostly due to impaction on the bronchiole walls. For $Re < 1$, $\delta\bar{L} \sim Re^{-2}$. For $Re = 1$ the velocity of the flow is in $\sim \mathcal{O}(10^{-2})$ m/s which causes sedimentation of particles and increases δ by an order of magnitude. Further reduction of Re causes the suction velocity to be small enough that diffusion becomes the dominant mode of deposition. In addition, $\delta\bar{L}$ increases several orders of magnitude as Re is decreased from 10^3 to 10^{-2} i.e. from the impaction regime to the diffusion regime. The order of $\delta\bar{L}$ is almost constant in the impaction regime while it increases for $Re < 1$. Data from the literature has also been re-plotted in the current nomenclature in this figure. Firstly, it can be seen that at any value of Re , there is significant variation in the data from the literature. Secondly, the data in the literature is limited to values of $Re > 10^2$. It can be seen from the figure 4.4 (b), that our data is within the range of values from the literature. This can be noted as the most important finding of this study that is hardly available in the existing literature.



(a)



(b)

Figure 4.4: (a) Plot of \bar{D}_F versus Re . Re varies over five orders of magnitude of mimicking flow conditions in different generations of the lung. The deposition fraction per unit tubule length and per unit suction time represented by D_F shows the lowest value when $Re = 1$, for $\bar{L} = 50$ and 150 . According to the deposition mechanism of aerosols three zones are identified as follows: deposition by *impaction* ($10 < Re \leq 10^3$), deposition by *sedimentation* ($10 < Re < 1$), deposition by *diffusion* ($10^{-3} \leq Re < 1$). (b) Plot of $\delta\bar{L}$ versus Re for \bar{D} being constant at 77 and for $\bar{L} = 50$ and 150 . Re varies over five orders of magnitude. The data in figure 4.4 (a) collapses onto a single curve when re-scaled as above. Interestingly, $\delta\bar{L} \sim Re^{-2}$ for $Re < 1$ and is constant for $Re > 1$. In the plot green dotted line is the best fit for $Re < 1$ given by $\delta\bar{L} = 1.55 \times 10^{-7} Re^{-2}$. Blue dotted line is the best fit for $Re > 1$ given by $\delta\bar{L} = 2.73 \times 10^{-7}$. Figure legend: \triangle Kim *et al.* (1984); \triangleleft Matsui *et al.* (1974); \square Tao *et al.* (2018); \star Ström (1972)

CHAPTER 5

Deposition Modelling

This chapter discusses the implications of the functional form of the deposition correlation G , from the experimental results for the equation 4.3. This is a physics-consistent, dimensionless deposition model that can be used to estimate the regional deposition in lungs for a given breathing condition and particle size.

5.1 Model development

A dimensionless deposition model is developed from the experimental results which is the main focus of this study. All the parameters influencing the deposition is considered in this study and non dimensional form of those parameters are used to develop the model so that the model can be used for all dimensional forms. Figures 5.1(a) and 5.1(b) are modified representations of figures 4.3(b) and 4.4(b) respectively. These figures represent the same phenomena as from the earlier figures but in terms of modified dimensionless parameters. Figure 5.1(a) shows that $\delta\bar{L}$ linearly scales to \bar{D}^3 and it is independent of particle Reynolds number ($Re\bar{D}$). In this case, $Re \gg 1$. Similar result is obtained from figure 4.4(b) as well as figure 5.1(b) where $\delta\bar{L}$ is independent of $Re\bar{D}$ for $Re \gg 1$. But for $Re \ll 1$, $\delta\bar{L}$ strongly depends on particle Reynolds number ($Re\bar{D}$) as indicated in figure 5.1(b). The collapse of data in Figures 5.1(a) and 5.1(b) points to a universal description of deposition in dimensionless terms as a function of \bar{D} and Re , the two abscissa parameters in these figures. The best fit to the data in figure 5.1(a) suggests that $\delta\bar{L} \sim \bar{D}^3$ for $Re \gg 1$ and independent of Re . Therefore, one can related $\delta\bar{L}$ to \bar{D} . A curve fit for the data pertaining to $Re \ll 1$ in figure 5.1(b) suggests that $\delta\bar{L} \sim (Re\bar{D})^{-2}$. By combining the two relations obtained from figures 5.1(a) and (b), a universal deposition equation is derived as follows.

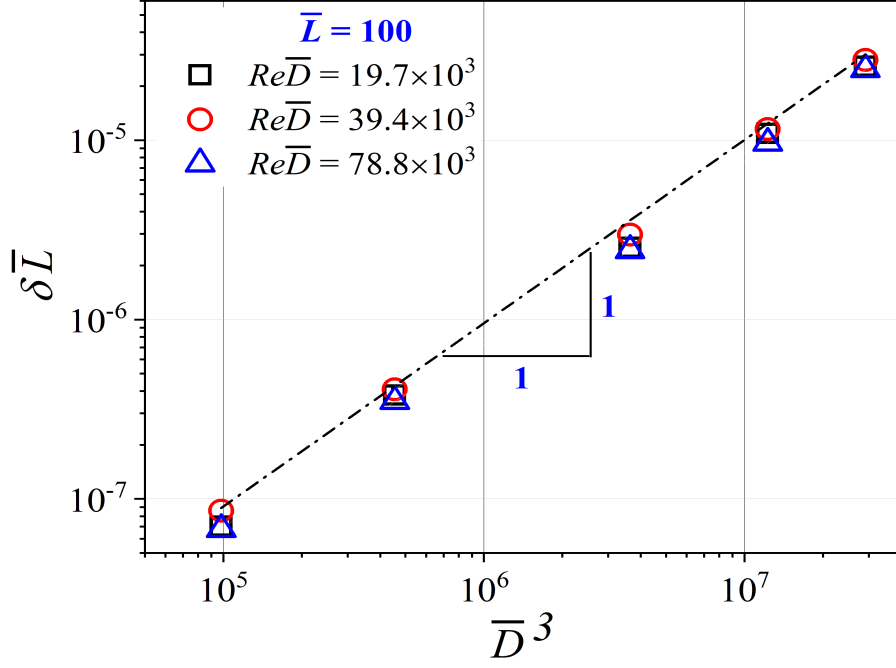
$$\delta\bar{L} = 7 \times 10^{-13} \bar{D}^3 \quad \text{if } Re \gg 1 \quad (5.1a)$$

$$= 1.55 \times 10^{-7} Re^{-2} \quad \text{if } Re \ll 1 \quad (5.1b)$$

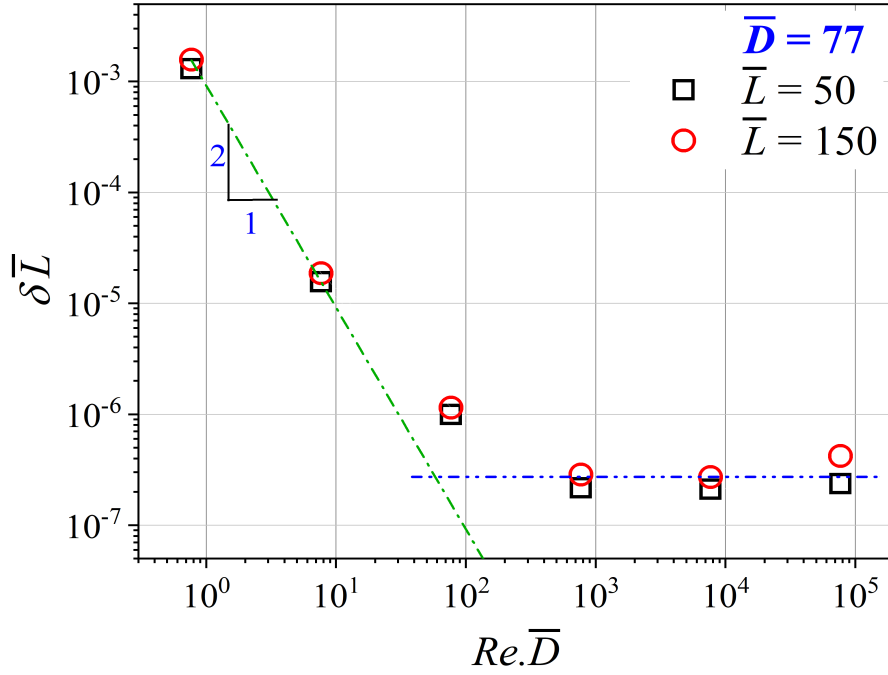
The equations 5.1 explain the data in both the figures 5.1(a) and (b). This is the explicit form of equation 4.3 that we set out to identify. Equations 5.1 also indicate the minimal set of dimensionless parameters that are required to model aerosol deposition over the entire range of lung-relevant operating conditions.

In order to understand the physics underlying equations 5.1, it is useful to recast equations 5.1 back into the dimensional parameter form. From the dimensional form of equation 5.1a for $Re \ll 1$, we find that $d \propto \nu^2 T^2 \alpha_0 / D_{10}$. Recall that d is defined as the total volume of aerosol deposited in time T . For $Re \ll 1$, as expected, the flow rate and other parameters do not play a role. The deposition depends linearly on the particle concentration α_0 . The rate of deposition is proportional to D_{10}^{-1} as one would expect in diffusion-dominated deposition (since the diffusion coefficient scales as D_{10}^{-1}). From the dimensional form of equation 5.1b for $Re \gg 1$, we find that $d \propto Q^2 T^2 \alpha_0 / D_{10}^3$. Again, as expected, the deposition in this case is dependent on the square of the velocity (Q^2) and depends linearly on the particle concentration (α_0), since d is dominated by impaction.

The experimentally developed model is validated for breathing cycle of 4 seconds and $D_{10} \sim \mathcal{O}(10\mu m)$ with the results obtained by Hinds (1999). The figure 5.2(a) shows the deposition for different lungs generations estimated from the model. It is calculated from the model that among total deposition of 88.6%, the deposition in conducting zone is 87.64% and in respiratory zone is 1.025% which matches well from the result of Hinds (1999) as shown in figure 5.2(b).

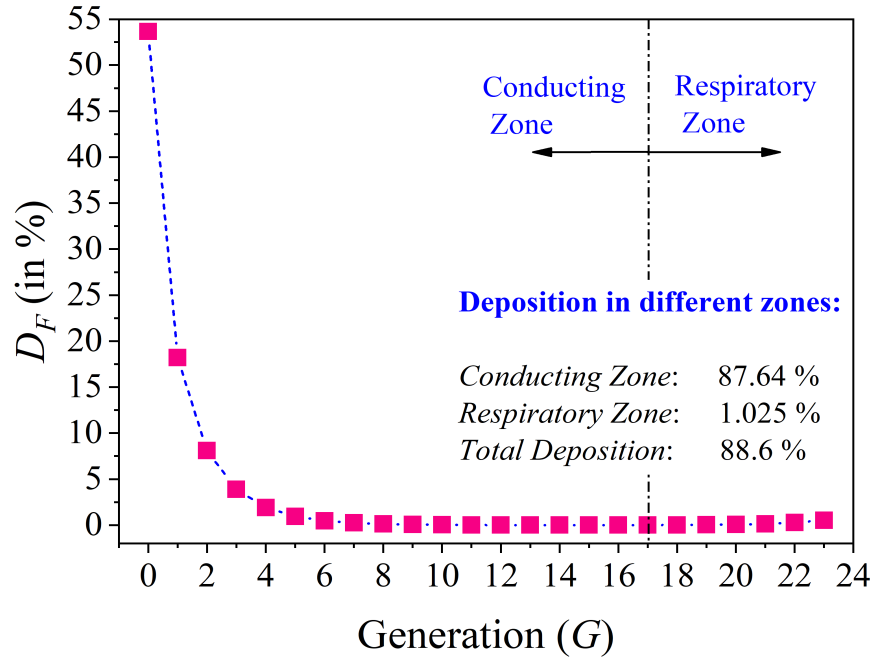


(a)

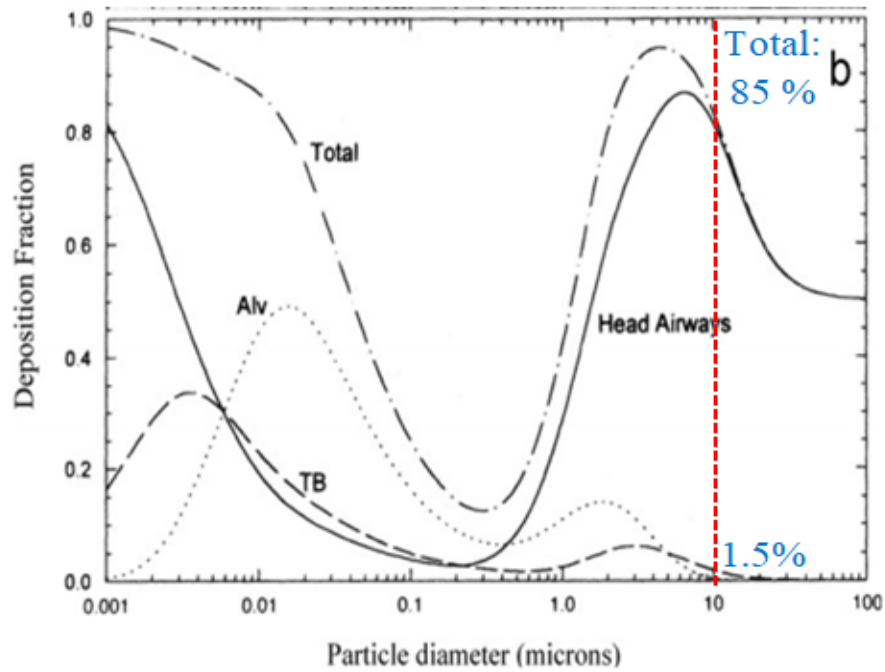


(b)

Figure 5.1: (a) Modified representation of figure 4.3(b). The same data is re-plotted to show the variation of $\delta\bar{L}$ versus \bar{D}^3 . The best fit power law is given by $\delta\bar{L} = 7 \times 10^{-13}\bar{D}^3$. The fit is independent of $Re\bar{D}$. $Re \sim 10^3$ for all data in these plots implying impaction-dominated deposition. (b) Modified representation of figure 4.4(b) where $\delta\bar{L}$ is plotted against particle Reynolds number ($Re\bar{D}$ instead of flow Re). The best fit represented by green dotted line is given by $9 \times 10^{-4}(Re\bar{D})^{-2}$



(a)



(b)

Figure 5.2: (a) Plot of deposition fraction (D_F) versus lung generations (G) calculated from equation 5.1 for particle size $\sim \mathcal{O}(10\mu m)$ and breathing cycle of 4s. (b) Variation of deposition fraction with particle diameter given by Hinds (1999). The plot shows that for particle diameter of 10 micron the total deposition fraction is 83%, out of which 2% is deposited in alveolar and tracheobronchial region and remaining in the upper airways. This results matches well with model predicted deposition in plot (a)

5.2 Deposition calculation using the Model

The intention of developing the model from the experimental results is to calculate the regional deposition in lungs for estimating the efficacy of the delivered drug. The deposition fraction is calculated using the model (ref: figure 5.3 for single breathing cycle of 4 seconds (inspiration: 2s; expiration: 2s) and particle size $\sim \mathcal{O}(10\mu m)$, which is common among the commercially available nebulizers.

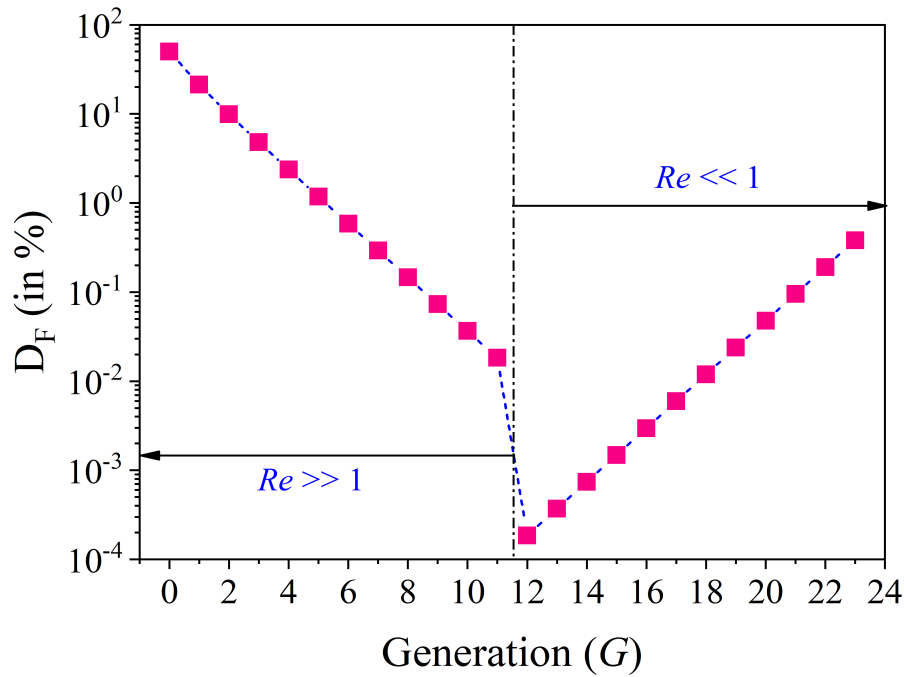


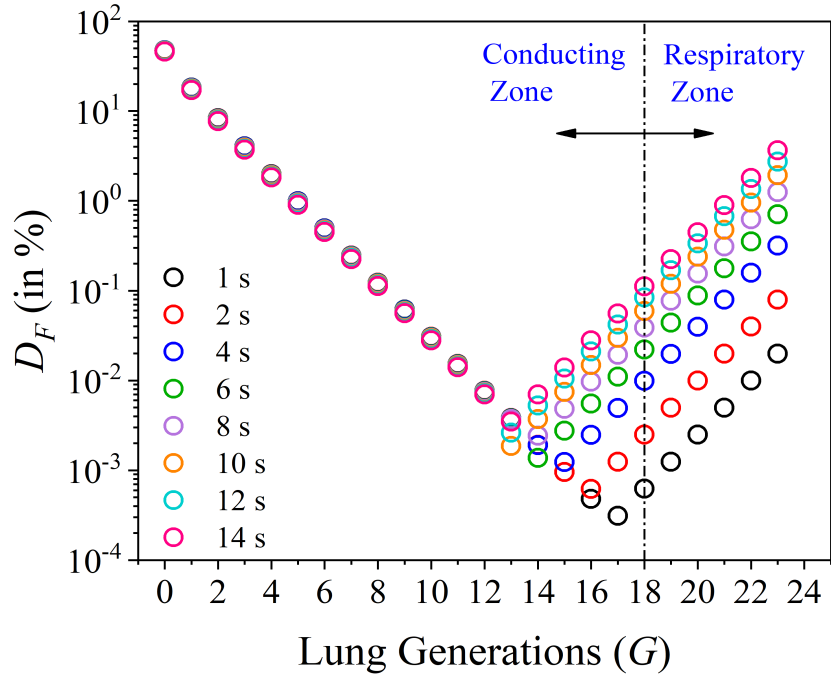
Figure 5.3: Plot of deposition fraction (D_F) and generation number, calculated using equation 5.1 for single breathing cycle (4s) and particle size $\sim \mathcal{O}(10\mu m)$. The plot is same as figure 5.2(a) with the abscissa in the log scale. The discontinuity of the plot after $G = 11$ is due to the change in deposition model from equation 5.1(a) to (b) resulted due to the change in Re .

In the figure 5.3 the deposition decreases exponentially from $0 \leq G \leq 11$ and rising exponentially for $12 \leq G \leq 23$. The discontinuity between generation 11 and 12 is due to the change of the deposition model. The deposition model in equation (5.1) is valid in the asymptotic limits of $Re \ll 1$ and $Re \gg 1$. The region near $Re \sim 1$ is a cross-over region where the equations are strictly not valid. This is the source of the discontinuity in Figure 5.3. The figure shows a total deposition fraction of 82.5% out of which 81.9% deposits in the air conducting zone and 0.6% is deposited in the respiratory zone of the lungs. This low deposition fraction in the respiratory zone i.e. $17 \leq G \leq 23$ reduces the efficacy of the drug since most of the inhaled particles deposits in the upper

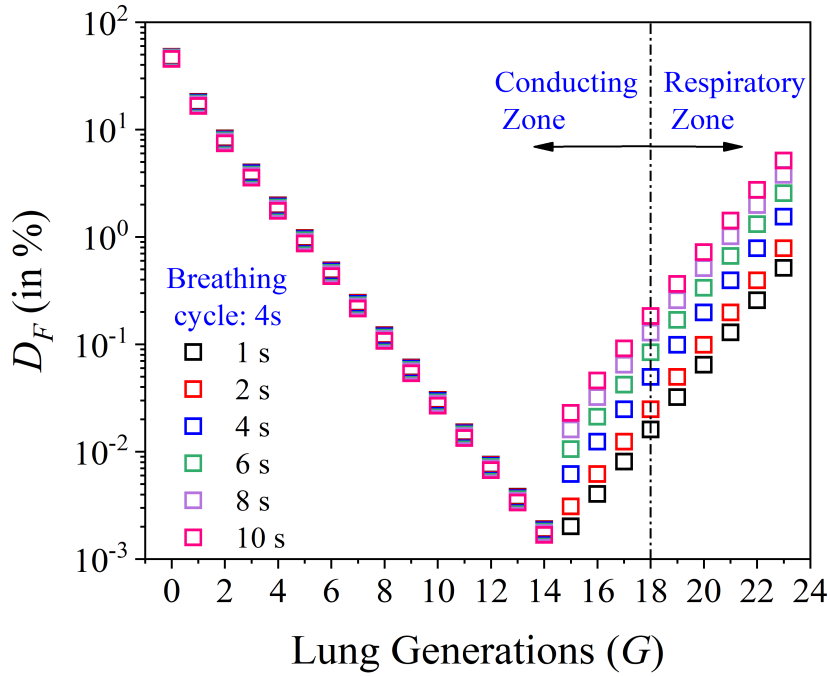
lungs where it cannot be introduced into the blood stream. Thus the equation 5.1 is a closed form expression to estimate the deposition in any bronchiole in the lung, given its geometry and flow properties. We have ignored orientation of the bronchiole, since we have only studied deposition in horizontal bronchioles. However, as pointed out by Goldberg (1981), one could account for the orientation angle by re-scaling time using the cosine of the angle of inclination.

The treatment of respiratory disease using nebulized drug finds its effectiveness when the drug deposits in the alveolar region of the lungs where gaseous exchanges takes place. The main goal of this study lies in estimating the regional deposition in the entire lung and increasing the amount of deposition in the alveolar region to increase drug efficacy. In this context, it is well-known that the breathing frequency and the breath hold time has a significant effect on aerosol deposition. The developed model is used to analyse the effect of breathing frequency and breath hold time for deposition of $10\mu m$ sized particles, for single breathing cycle. Figure 5.4(a) shows the effect of breathing frequency on regional deposition in lungs. The regional deposition fraction is analysed for different duration of breathing cycle (inspiration and expiration) ranging from $1s - 14s$. The variation of breathing frequency is mainly due to different types of activities we do round the day. The breathing cycle of $1s$ (inspiration: $0.5s$ and expiration: $0.5s$) takes place at the time of intense activity like running, swimming, cycling, climbing and other different workouts. The breathing cycle of $2s$ represents moderate activities like walking, light work outs etc and the cycle of $4s$ represents sedentary activities like sitting, lying down etc, which also represents the normal breathing cycle of human adult. From the figure it can be seen that for intense activity the deposition in the alveolar region region is significantly low and the total deposition in lungs is decreased. With a decrease in breathing frequency the deposition for $Re < 1$ increases whereas the deposition for $Re > 1$ is constant. This is because the model for $Re \ll 1$ (ref: equation 5.1) indicates that the dimensionless deposition is proportional to Re^{-2} whereas for $Re \gg 1$, the deposition is independent of Re . Thus lower breathing frequency increases deposition in the alveolar region of the lungs due to high residence time of the aerosol which enhances the diffusion process and is desirable for high drug efficiency. The alveolar deposition can be further increased by introducing the breath hold time between inspiration and expiration. The figure 5.4(b) shows the effect of breath hold time on alveolar deposition for breathing cycle of $4s$ and particle diameter of $10\mu m$.

The breath hold time contributes to the diffusion deposition process ($Re < 1$) which is dominant in the alveolar region in turn increasing aerosol deposition in the alveolus. The figure 5.5 shows that the increase in alveolar deposition is non-linear with breathing frequency ($D_F \sim T^2$). Thus the increase of alveolar deposition becomes insignificant after certain duration of breathing cycle. But the alveolar deposition linearly increases with the breath hold time ($D_F \sim T^{1.2}$) which indicates that longer breath hold time can increase the chances of virus infection significantly and at the same time it is desirable for higher drug deposition. The figure 5.5 shows that the increase in alveolar deposition is non-linear with breathing frequency ($D_F \sim T^{1.96}$). Thus the increase of alveolar deposition becomes insignificant after certain duration of breathing cycle. But the alveolar deposition linearly increases with the breath hold time ($D_F \sim T^{1.16}$) which indicates that longer breath hold time can increase the effects of drugs significantly. The effect of breath hold time is more significant than that of breathing frequency. Since both the curves are diverging with time (ref: figure 5.5), it can be inferred that higher breath hold time can be dangerous in terms of getting infected from the virus laden droplets. The addition of lower breathing frequency (i.e increase in inspiration and expiration time) can also cause the situation to worsen as it increases the residence time of the infected particles in the distal lung airways. The increase in the residence time will enhance the deposition in the alveolar airways since the diffusive deposition, which is the dominant mechanism in the distal lung, is directly proportional to time. Therefore, in addition to a lower breathing frequency, introduction of breath hold time in between inhalation and exhalation can increase the threat of virus infection in a crowded place. On other hand, in addition to a lower breathing frequency, breath hold time can be introduced in between inhalation and exhalation to maximise alveolar deposition and thus increase drug efficacy.



(a)



(b)

Figure 5.4: (a) Plot of D_F and lung generations (G) for different breathing frequency. The time for each breathing cycle is considered as time for inspiration and expiration together. (b) Plot of D_F and G for different breath hold time. For both the plots it can be seen that model for $Re \gg 1$ do not show any response with breathing frequency and breath hold time, whereas the model for $Re \ll 1$ found to be very sensitive for both of these parameters.

In conclusion, we have developed a quantitative physics-consistent correlation to predict the rate of deposition in any bronchiole of the lung. This model can now become the building block to developing a model for the total and regional deposition in the lung. One could construct a branching tree structure of the distal branching structure and model total deposition as a sum of all the bronchiole deposition. This modeling approach is grounded in experiments and could be construed to be complementary to purely computational whole lung simulation (Koullapis *et al.*, 2020) approaches that are being pursued in the recent literature.

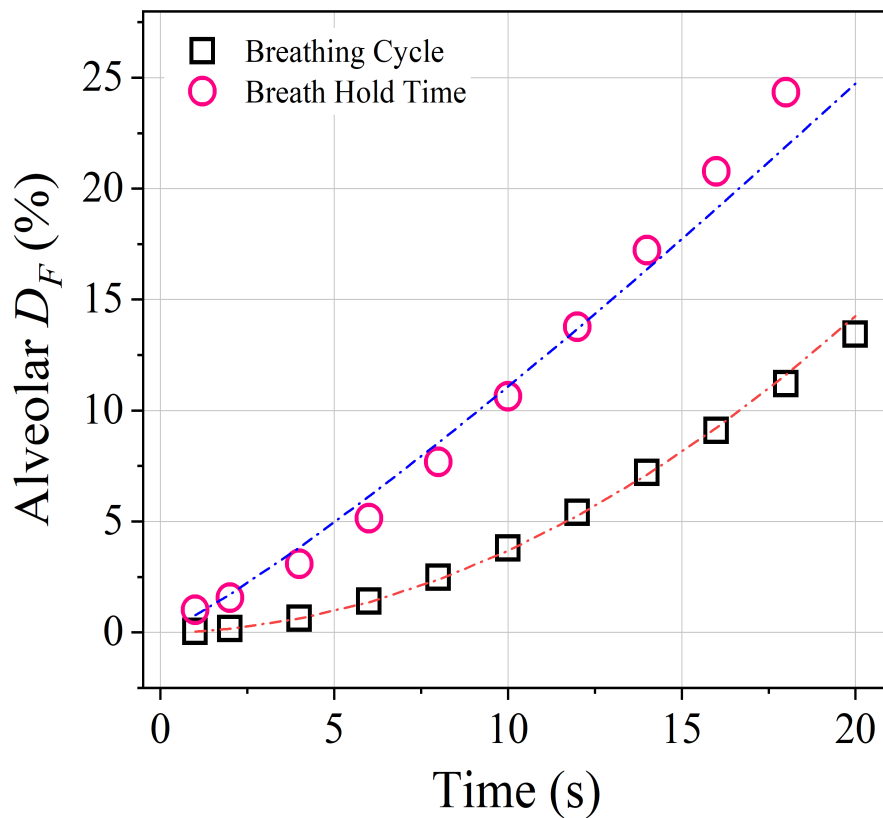


Figure 5.5: Plot of variation of alveolar deposition fraction (D_F) with time for different breathing frequency and breath hold time. The alveolar D_F scales to T^2 for breathing cycle (Blue dotted line: $D_F = 0.04T^{1.96}$ and scale to T for breath hold time (Red dotted line: $0.766T^{1.16}$)

CHAPTER 6

Conclusion and Future Scope

This chapter briefly lists out the key observations, understandings and conclusions from this study. It also discusses the future scope of this work which will provide deeper understanding of this study in order to improve the deposition model.

6.1 Conclusion

An experimental study of aerosol deposition in phantom bronchioles has been carried out for a wide range of Reynolds numbers ($10^{-2} < Re < 10^3$) and different bronchiole diameters ranging from $0.3\text{mm} - 2\text{mm}$ as well as for differing aspect ratios of the bronchiole. The experiments closely replicate flow and aerosol characteristics in the different generations of bronchioles in the lung. The aerosols were generated using an ultrasonic nebulizer, producing a mean droplet size $6.5\mu\text{m}$. The aerosol particles were doped with boron quantum dots, the deposition of which was quantified by spectrofluorometer. The following conclusions can be drawn from the study:

1. The dimensionless deposition in a particular bronchiole (δ) is inversely proportional to the aspect ratio of the bronchiole (\bar{L}) (ref. figure 4.1) but the effect of Re diminishes with increasing \bar{L} .
2. The value of δ increases exponentially with an increase in the dimensionless diameter (\bar{D}) for different \bar{L} . In addition, δ decreases with an increase in \bar{L} for all \bar{D} . However, the variation of δ with \bar{L} is small compared to its variation with \bar{D} .
3. The value of δ is independent of the particle size based Reynolds number ($Re\bar{D}$). For all $Re\bar{D}$, δ exhibits an exponential increase with \bar{D} .
4. $\delta\bar{L}$ is independent of \bar{L} over several orders of magnitude of Re , which confirms the inverse relation between δ and \bar{L} in figure 4.1.
5. For low Re , $\delta\bar{L} \sim Re^{-2}$, indicating that the amount of aerosol deposited is independent of the flow conditions and only depends of the aerosol conditions. This is the case with *diffusion* dominated deposition.
6. The parameter regime where $10^{-1} < Re < 10$ is identified as the zone where *sedimentation* is dominant.

7. $\delta\bar{L}$ is independent of Re for $10 < Re < 10^3$ which is identified as the *impaction* regime.
8. The deposition model is developed using the experimental data (see equation 5.1). The model predicts deposition fraction of 81.88 % in the conducting airways ($0 \leq G \leq 17$) and 0.624 % in the respiratory airways ($18 \leq G \leq 23$) for particle size $\sim \mathcal{O}(10\mu m)$ which matches well with the results of Hinds (1999).
9. The breathing frequency and the breath hold time have significant effect on alveolar deposition. The drug delivery efficiency can be increased with low breathing frequency and by introducing high breath hold time between inspiration and expiration.

6.2 Future scope

This work is a fundamental deposition study that leads to understand the combined effects of different parameters influencing aerosol deposition in straight tubes. The quantitative analysis of deposition in micro capillaries is a challenging task which is addressed in this work by using Boron quantum dots as fluorescence aerosol. Although this study reports deposition in alveolar dimension capillaries with wide ranges of Re mimicking the whole lungs, still there exists lots of future scopes for this work. This study can be extended in future in the following ways:

1. This study is performed with straight tubes for wide ranges of diameters. But the bifurcations of the lung bronchioles may play a significant role in deposition. Thus experiments can be carried out with "Y - shape" bifurcated tubes in future for development of better model.
2. This study is restricted to suction of aerosol at a particular rate. The experimental setup can be modified to suck in and pump out mode as occurs in real breathing condition.
3. The effect of gravity is not studied in this work although they affects the deposition process (Goldberg, 1981). Thus the effect of different parameters can be studied in both horizontal and vertical capillaries to make the deposition model more rigid.
4. This study is done with poly-dispersed aerosol with mean size of $6.5\mu m$ which is common with commercially available nebulizers. Thus further investigations can be carried out with mono-dispersed particles of different sizes to study the effect of particle size on deposition, explicitly.

APPENDIX A

MATLAB code for global pdf

```
clc
clear all

% read data

str1 = 'Nebulizer'
Nrad =7;
width=2;
nbin=100;

for k=1:Nrad
newstr = sprintf('%0.1d',k-1);
Filename = strcat(str1, newstr, '.csv');
diak,1 = xlsread(Filename,'C:C');
velk,1 = xlsread(Filename,'B:B');
end

%% area calculation
rstart = -((Nrad-1)/2)*width;
rend = ((Nrad-1)/2)*width;

for i=1:Nrad
radloc(i)=rstart+(i-1)*width;
end

for i=1:Nrad
area(i)=1/2*abs(pi*(radloc(i)+width/2)^2-pi*(radloc(i)-width/2)^2);
```

```

end
area(((Nrad-1)/2)+1)=pi*(width/2)^2; % Area at center location

%% max & min size and velocity calculation to set axis

maxdrop=0;
mindrop=1000;
globalD=zeros(1,1);
globalA=zeros(1,1);
for i=1:Nrad
temp = diai,1;
maxdrop1=max(temp);
maxdrop=max(maxdrop1,maxdrop);
mindrop1=min(temp);
mindrop=min(mindrop1,mindrop);
end
[ sg dummy ] = size(globalD);
globalD=globalD(2:sg,1);
globalA=globalA(2:sg,1);
globalA=int16(globalA);

```

```
clear temp
```

```

maxvel=0;
minvel=100;
globalV=zeros(1,1);
for i=1:Nrad
temp = veli,1;
maxvel1=max(temp);
maxvel=max(maxvel1,maxvel);
minvel1=min(temp);
minvel=min(minvel1,minvel);

```

```

end
[ sg dummy ] =size(globalV);
globalV=globalV(2:sg,1);

clear temp

%% bining method for size and velocity pfd calculation

grat=(maxdrop/mindrop)^(1/nbin);
X=mindrop*grat.^(0:nbin);
X(1)=mindrop*0.5; % Geometric progression of bins
X(nbin+1)=maxdrop*1.1;

% A=(1.02*maxdrop-0.5*mindrop)/nbin;
B=(1.02*maxvel-1.01*minvel)/nbin;
% X=[0.5*mindrop:A:maxdrop*1.02]; % Arithmetic progression of bins
Y=[1.01*minvel:B:maxvel*1.02];

%% diameter pdf calculation

N1=zeros(1,nbin+1);
N2=zeros(1,nbin+1);
for i=1:Nrad
temp = diai,1;
[ stemp dummy ] =size(temp);
temp1=temp(:,1);
[ N1,y1 ] =hist(temp1,X);
N2=N1*area(i)+N2;
end
clear temp
clear temp1

```

```

    N2=N2/sum(N2);
normfac=trapz(X,N2);
N2=N2/normfac;

%% velocity pdf calculation

    N3=zeros(1,nbin+1);
N4=zeros(1,nbin+1);
for i=1:Nrad
temp = veli,1;
[ stemp dummy ] =size(temp);
temp1=temp(:,1);
[ N3,y1 ] =hist(temp1,Y);
N4=N3*area(i)+N4;
end

    N4=N4/sum(N4);
normfac=trapz(Y,N4);
N4=N4/normfac;

%%
figure(1)
scrsz = get(0,'ScreenSize');
h = gcf;
set(h,'Position',[0 0 2000 1000]);
plot(X,N2,'ks','LineWidth',2.5,'MarkerEdgeColor','k','MarkerSize',15)
xlabel(' x ', 'Interpreter','latex','FontWeight','bold','FontSize',35,'FontName','Times new
romen');
ylabel('  $\mathcal{X}(x)$  ', 'interpreter','latex','rot',90,'FontWeight','bold','FontSize',35,'FontName','Times
new romen');

```

```

%%
figure(2)
scrsz = get(0,'ScreenSize');
h = gcf;
set(h,'Position',[0 0 2000 1000]);
plot(Y,N4,'ks','LineWidth',2.5,'MarkerEdgeColor','k','MarkerSize',15)
xlabel('u','Interpreter','latex','FontWeight','bold','FontSize',35,'FontName','Times new
romen');
ylabel('U(u)','interpreter','latex','rot',90,'FontWeight','bold','FontSize',35,'FontName','Times
new romen');

hold off;

```

REFERENCES

1. **Ananthanarayanan, A., X. Wang, P. Routh, B. Sana, S. Lim, D.-H. Kim, K.-H. Lim, J. Li, and P. Chen** (2014). Facile synthesis of graphene quantum dots from 3d graphene and their application for fe³⁺ sensing. *Advanced Functional Materials*, **24**(20), 3021–3026.
2. **Asgharian, B., W. Hofmann, and R. Bergmann** (2001). Particle deposition in a multiple-path model of the human lung. *Aerosol Science & Technology*, **34**(4), 332–339.
3. **Asgharian, B., M. Menache, and F. Miller** (2004). Modeling age-related particle deposition in humans. *Journal of aerosol medicine*, **17**(3), 213–224.
4. **Asgharian, B. and O. Price** (2006). Airflow distribution in the human lung and its influence on particle deposition. *Inhalation Toxicology*, **18**(10), 795–801.
5. **Baker, M.** (2011). A living system on a chip. *Nature*, **471**(7340), 661–665.
6. **Bennett, G., M. Joyce, L. Sweeney, and R. MacLoughlin** (2019). In vitro study of the effect of breathing pattern on aerosol delivery during high-flow nasal therapy. *Pulmonary Therapy*, **5**(1), 43–54.
7. **Brand, P., I. Friemel, T. Meyer, H. Schulz, J. Heyder, and K. Häußinger** (2000). Total deposition of therapeutic particles during spontaneous and controlled inhalations. *Journal of pharmaceutical sciences*, **89**(6), 724–731.
8. **Chakravarty, A., N. A. Patankar, and M. V. Panchagnula** (2019). Aerosol transport in a breathing alveolus. *Physics of Fluids*, **31**(12), 121901.
9. **Cheng, Y. S.** (2014). Mechanisms of pharmaceutical aerosol deposition in the respiratory tract. *AAPS PharmSciTech*, **15**(3), 630–640.
10. **Clark, A.** (2004). Pulmonary deliver technology: recent advances and potential for the new millenium. *Pharmaceutical inhalation aerosol technology*.
11. **Dames, P., B. Gleich, A. Flemmer, K. Hajek, N. Seidl, F. Wiekhorst, D. Eberbeck, I. Bittmann, C. Bergemann, T. Weyh, et al.** (2007). Targeted delivery of magnetic aerosol droplets to the lung. *Nature nanotechnology*, **2**(8), 495.
12. **Darquenne, C., W. J. Lamm, J. M. Fine, R. A. Corley, and R. W. Glenny** (2016). Total and regional deposition of inhaled aerosols in supine healthy subjects and subjects with mild-to-moderate copd. *Journal of aerosol science*, **99**, 27–39.
13. **DeHaan, W. H. and W. H. Finlay** (2001). In vitro monodisperse aerosol deposition in a mouth and throat with six different inhalation devices. *Journal of Aerosol Medicine*, **14**(3), 361–367.
14. **Deng, Q., L. Deng, Y. Miao, X. Guo, and Y. Li** (2019a). Particle deposition in the human lung: Health implications of particulate matter from different sources. *Environmental research*, **169**, 237–245.

15. **Deng, Q., C. Ou, Y.-M. Shen, Y. Xiang, Y. Miao, and Y. Li** (2019b). Health effects of physical activity as predicted by particle deposition in the human respiratory tract. *Science of The Total Environment*, **657**, 819–826.
16. **Devi, S. K., M. V. Panchagnula, and M. Alladi** (2016). Designing aerosol size distribution to minimize inter-subject variability of alveolar deposition. *Journal of Aerosol Science*, **101**, 144–155.
17. **Dhivyaraja, K., D. Gaddes, E. Freeman, S. Tadigadapa, and M. Panchagnula** (2019). Dynamical similarity and universality of drop size and velocity spectra in sprays. *Journal of Fluid Mechanics*, **860**, 510–543.
18. **Dolovich, M.** (2001). Measuring total and regional lung deposition using inhaled radiotracers. *Journal of Aerosol Medicine*, **14**(1, Supplement 1), 35–44.
19. **Esch, M., T. King, and M. Shuler** (2011). The role of body-on-a-chip devices in drug and toxicity studies. *Annual review of biomedical engineering*, **13**, 55–72.
20. **Fan, S., L. Ding, and K. Yao** (2013). Electronic structure and ferromagnetism of boron doped bulk and surface cdse: By generalized gradient approximation and generalized gradient approximation plus modified becke and johnson calculations. *Journal of Applied Physics*, **114**(11), 113905.
21. **Ferron, G.** (1977). Deposition of polydisperse aerosols in two glass models representing the upper human airways. *Journal of aerosol Science*, **8**(6), 409–427.
22. **Ferron, G.** (1994). Aerosol properties and lung deposition. *European Respiratory Journal*, **7**(8), 1392–1394.
23. **Fishler, R., P. Hofemeier, Y. Etzion, Y. Dubowski, and J. Sznitman** (2015). Particle dynamics and deposition in true-scale pulmonary acinar models. *Scientific reports*, **5**, 14071.
24. **Fishler, R., Y. Ostrovski, C.-Y. Lu, and J. Sznitman** (2017). Streamline crossing: An essential mechanism for aerosol dispersion in the pulmonary acinus. *Journal of biomechanics*, **50**, 222–227.
25. **Fox, S.**, *Human physiology*. McGraw-Hill Education, 2015.
26. **Friedlander, S. and H. Johnstone** (1957). Deposition of suspended particles from turbulent gas streams. *Industrial & Engineering Chemistry*, **49**(7), 1151–1156.
27. **Glover, W., H.-K. Chan, S. Eberl, E. Daviskas, and J. Verschuer** (2008). Effect of particle size of dry powder mannitol on the lung deposition in healthy volunteers. *International journal of pharmaceuticals*, **349**(1-2), 314–322.
28. **Goldberg, I. S.** (1981). Settling and diffusion of aerosol particles in small airways during breath holding. *Annals of Biomedical Engineering*, **9**, 557–575.
29. **Grgic, B., W. Finlay, and A. Heenan** (2004). Regional aerosol deposition and flow measurements in an idealized mouth and throat. *Journal of Aerosol Science*, **35**(1), 21–32.
30. **Grotberg, J. B.** (2011). Respiratory fluid mechanics. *Physics of Fluids*, **23**(2), 021301.

31. **Hansen, J. E.** and **E. P. Ampaya** (1975). Human air space shapes, sizes, areas, and volumes. *Journal of Applied Physiology*, **38**(6), 990–995.
32. **Heyder, J., J. Gebhart, G. Rudolf, C. F. Schiller,** and **W. Stahlhofen** (1986). Deposition of particles in the human respiratory tract in the size range 0.005–15 μm . *Journal of aerosol science*, **17**(5), 811–825.
33. **Hinds, W. C.**, *Aerosol technology: properties, behavior, and measurement of airborne particles*. John Wiley & Sons, 1999.
34. **Hofemeier, P.** and **J. Sznitman** (2016). The role of anisotropic expansion for pulmonary acinar aerosol deposition. *Journal of biomechanics*, **49**(14), 3543–3548.
35. **Hofmann, W.** and **L. Koblinger** (1990). Monte carlo modeling of aerosol deposition in human lungs. part ii: Deposition fractions and their sensitivity to parameter variations. *Journal of Aerosol Science*, **21**(5), 675–688.
36. **Hofmann, W., E. Pawlak,** and **R. Sturm** (2008). Semi-empirical stochastic model of aerosol bolus dispersion in the human lung. *Inhalation toxicology*, **20**(12), 1059–1073.
37. **Horsfield, K.** and **G. Cumming** (1968). Morphology of the bronchial tree in man. *Journal of applied physiology*, **24**(3), 373–383.
38. **Horsfield, K., G. Dart, D. E. Olson, G. F. Filley,** and **G. Cumming** (1971). Models of the human bronchial tree. *Journal of applied physiology*, **31**(2), 207–217.
39. **Huh, D., B. D. Matthews, A. Mammoto, M. Montoya-Zavala, H. Y. Hsin,** and **D. E. Ingber** (2010). Reconstituting organ-level lung functions on a chip. *Science*, **328**(5986), 1662–1668.
40. **Jaques, P. A.** and **C. S. Kim** (2000). Measurement of total lung deposition of inhaled ultrafine particles in healthy men and women. *Inhalation toxicology*, **12**(8), 715–731.
41. **Jayaraju, S., M. Brouns, C. Lacor, B. Belkassam,** and **S. Verbanck** (2008). Large eddy and detached eddy simulations of fluid flow and particle deposition in a human mouth–throat. *Journal of Aerosol Science*, **39**(10), 862–875.
42. **Khajeh-Hosseini-Dalasm, N.** and **P. W. Longest** (2015). Deposition of particles in the alveolar airways: inhalation and breath-hold with pharmaceutical aerosols. *Journal of aerosol science*, **79**, 15–30.
43. **Kim, C. S., G. G. Lewars, M. A. Eldridge,** and **M. A. Sackner** (1984). Deposition of aerosol particles in a straight tube with an abrupt obstruction. *Journal of aerosol science*, **15**(2), 167–176.
44. **Kleinstreuer, C.** and **Z. Zhang** (2010). Airflow and particle transport in the human respiratory system. *Annual review of fluid mechanics*, **42**, 301–334.
45. **Kleinstreuer, C., Z. Zhang,** and **J. Donohue** (2008). Targeted drug-aerosol delivery in the human respiratory system. *Annu. Rev. Biomed. Eng.*, **10**, 195–220.
46. **Kline, S. J.** (1953). Describing uncertainty in single sample experiments. *Mech. Engineering*, **75**, 3–8.

47. **Kolanjiyil, A. V.** and **C. Kleinstreuer** (2016). Computationally efficient analysis of particle transport and deposition in a human whole-lung-airway model. part i: Theory and model validation. *Computers in biology and medicine*, **79**, 193–204.
48. **Kolanjiyil, A. V.** and **C. Kleinstreuer** (2017). Computational analysis of aerosol-dynamics in a human whole-lung airway model. *Journal of Aerosol Science*, **114**, 301–316.
49. **Kolanjiyil, A. V.**, **C. Kleinstreuer**, and **R. T. Sadikot** (2017). Computationally efficient analysis of particle transport and deposition in a human whole-lung-airway model. part ii: Dry powder inhaler application. *Computers in biology and medicine*, **84**, 247–253.
50. **Koullapis, P.**, **P. Hofemeier**, **J. Sznitman**, and **S. C. Kassinos** (2018). An efficient computational fluid-particle dynamics method to predict deposition in a simplified approximation of the deep lung. *European Journal of Pharmaceutical Sciences*, **113**, 132–144.
51. **Koullapis, P.** and **S. C. Kassinos**, The effect of flow rate and electrostatic charge on aerosol deposition in a realistic lung geometry. *In Direct and Large-Eddy Simulation X*. Springer, 2018, 343–349.
52. **Koullapis, P.**, **F. Stylianou**, **J. Sznitman**, **B. Olsson**, and **S. Kassinos** (2020). Towards whole-lung simulations of aerosol deposition: a model of the deep lung. *Journal of Aerosol Science*, 105541.
53. **Levitzky, M.** (2007). Nonrespiratory functions of the lung. *Pulmonary Physiology*. New York: McGraw Hill, 217–220.
54. **Li, W.-I.** and **D. A. Edwards** (1997). Aerosol particle transport and deaggregation phenomena in the mouth and throat. *Advanced drug delivery reviews*, **26**(1), 41–49.
55. **Lin, C.-K.**, **Y.-Y. Hsiao**, **P. Nath**, and **J.-H. Huang** (2019). Aerosol delivery into small anatomical airway model through spontaneous engineered breathing. *Biomicrofluidics*, **13**(4), 044109.
56. **Lippmann, M.** and **R. E. Albert** (1969). The effect of particle size on the regional deposition of inhaled aerosols in the human respiratory tract. *American Industrial Hygiene Association Journal*, **30**(3), 257–275.
57. **Lizal, F.**, **M. Belka**, **J. Adam**, **J. Jedelsky**, and **M. Jicha** (2015). A method for in vitro regional aerosol deposition measurement in a model of the human tracheobronchial tree by the positron emission tomography. *Proceedings of the Institution of Mechanical Engineers, Part H: Journal of Engineering in Medicine*, **229**(10), 750–757.
58. **Longest, P. W.**, **M. Hindle**, **S. D. Choudhuri**, and **J. Xi** (2008). Comparison of ambient and spray aerosol deposition in a standard induction port and more realistic mouth–throat geometry. *Journal of Aerosol Science*, **39**(7), 572–591.
59. **Longest, P. W.** and **S. Vinchurkar** (2007). Validating cfd predictions of respiratory aerosol deposition: effects of upstream transition and turbulence. *Journal of biomechanics*, **40**(2), 305–316.

60. **Mackay, F. C., R. G. Roth, N. van Helmond, and T. K. Ben-Jacob** (2020). Computed tomography lung volume estimation to facilitate protective mechanical ventilation in a patient with achondroplasia and spina bifida. *Anaesthesia and Intensive Care*, **47**(5), 474–475.
61. **Madureira, J., K. Slezakova, A. I. Silva, B. Lage, A. Mendes, L. Aguiar, M. C. Pereira, J. P. Teixeira, and C. Costa** (2020). Assessment of indoor air exposure at residential homes: Inhalation dose and lung deposition of pm10, pm2.5 and ultrafine particles among newborn children and their mothers. *Science of The Total Environment*, **717**, 137293.
62. **Malet, J., L. Alloul, N. Michielsen, D. Boulaud, and A. Renoux** (2000). Deposition of nanosized particles in cylindrical tubes under laminar and turbulent flow conditions. *Journal of aerosol science*, **31**(3), 335–348.
63. **Mallik, A. K., T. P. Sarma, A. Roy, M. V. Panchagnula, and S. Seshadri** (2020). Phase doppler particle analyser (pdpa) characterization and modeling of sprays from orthogonally interacting water and air jets. *Journal of Flow Visualization and Image Processing*, **27**(2).
64. **Malvè, M., C. Sánchez-Matás, and J. L. López-Villalobos** (2020). Modelling particle transport and deposition in the human healthy and stented tracheobronchial airways. *Annals of Biomedical Engineering*, 1–16.
65. **Manshadi, M. K., M. Saadat, M. Mohammadi, R. Kamali, M. Shamsi, M. Naseh, and A. Sanati-Nezhad** (2019). Magnetic aerosol drug targeting in lung cancer therapy using permanent magnet. *Drug delivery*, **26**(1), 120–128.
66. **Matsui, H., Y. Yoshida, M. Murata, and T. Ohata** (1974). Measurement of deposition fraction of aerosol particles in a horizontal straight metal pipe. *Journal of Nuclear Science and Technology*, **11**(7), 300–307. URL www.scopus.com.
67. **Mauroy, B., M. Filoche, E. Weibel, and B. Sapoval** (2004). An optimal bronchial tree may be dangerous. *Nature*, **427**(6975), 633–636.
68. **Mi, Q., D. Chen, J. Hu, Z. Huang, and J. Li** (2013). Nitrogen-doped graphene/cds hollow spheres nanocomposite with enhanced photocatalytic performance. *Chinese Journal of Catalysis*, **34**(11), 2138–2145.
69. **Mitchell, D., M. Solomon, S. Tolfree, M. Short, and S. Spiro** (1987). Effect of particle size of bronchodilator aerosols on lung distribution and pulmonary function in patients with chronic asthma. *Thorax*, **42**(6), 457–461.
70. **Moffat, R. J.** (1988). Describing the uncertainties in experimental results. *Experimental thermal and fluid science*, **1**(1), 3–17.
71. **Montgomery, T. L. and M. Corn** (1970). Aerosol deposition in a pipe with turbulent airflow. *Journal of Aerosol Science*, **1**(3), 185–213.
72. **Moraes, C., G. Mehta, S. C. Lesher-Perez, and S. Takayama** (2012). Organs-on-a-chip: a focus on compartmentalized microdevices. *Annals of biomedical engineering*, **40**(6), 1211–1227.

73. **Muysshondt, A., N. Anand, and A. R. McFarland** (1996). Turbulent deposition of aerosol particles in large transport tubes. *Aerosol Science and Technology*, **24**(2), 107–116.
74. **Phalen, R., H. Yeh, G. Schum, and O. Raabe** (1978). Application of an idealized model to morphometry of the mammalian tracheobronchial tree. *The Anatomical Record*, **190**(2), 167–176.
75. **Phalen, R. F. and M. J. Oldham** (1983). Tracheobronchial airway structure as revealed by casting techniques. *American Review of Respiratory Disease*, **128**(2P2), S1–S4.
76. **Raabe, O.** (1976). Tracheobronchial geometry-human, dog, rat, hamster. *Lovelace Foundation for Medical Education and Research. Report number LF-53.*
77. **Reed, M. A., J. N. Randall, J. H. Luscombe, W. R. Frensley, R. J. Aggarwal, R. J. Matyi, T. M. Moore, and A. E. Wetsel**, Quantum dot resonant tunneling spectroscopy. *In Festkörperprobleme 29*. Springer, 1989, 267–283.
78. **Ricard, J.-D.** (2003). Are we really reducing tidal volume—and should we?
79. **Rostami, A. A.** (2009). Computational modeling of aerosol deposition in respiratory tract: a review. *Inhalation toxicology*, **21**(4), 262–290.
80. **Sehmel, G. A.** (1968). Aerosol deposition from turbulent airstreams in vertical conduits. Technical report, Battelle-Northwest, Richland, Wash. Pacific Northwest Lab.
81. **Semmler-Behnke, M., W. G. Kreyling, H. Schulz, S. Takenaka, J. P. Butler, F. S. Henry, and A. Tsuda** (2012). Nanoparticle delivery in infant lungs. *Proceedings of the National Academy of Sciences*, **109**(13), 5092–5097.
82. **Song, Z., T. Lin, L. Lin, S. Lin, F. Fu, X. Wang, and L. Guo** (2016). Invisible security ink based on water-soluble graphitic carbon nitride quantum dots. *Angewandte Chemie International Edition*, **55**(8), 2773–2777.
83. **Stahlhofen, W., J. Gebhart, and J. Heyder** (1980). Experimental determination of the regional deposition of aerosol particles in the human respiratory tract. *American Industrial Hygiene Association Journal*, **41**(6), 385–398a.
84. **Stapleton, K.-W., E. Guentsch, M. Hoskinson, and W. Finlay** (2000). On the suitability of $k-\epsilon$ turbulence modeling for aerosol deposition in the mouth and throat: a comparison with experiment. *Journal of Aerosol Science*, **31**(6), 739–749.
85. **Ström, L.** (1972). Transmission efficiency of aerosol sampling lines. *Atmospheric Environment (1967)*, **6**(2), 133–142.
86. **Svartengren, M., L. Linnman, K. Philipson, and P. Camner** (1987). Regional deposition in human lung of 2.5 μm particles. *Experimental lung research*, **12**(4), 265–279.
87. **Sznitman, J.** (2013). Respiratory microflows in the pulmonary acinus. *Journal of biomechanics*, **46**(2), 284–298.
88. **Tao, C., G. Zhao, S. Yu, W. Peng, and J. Wang** (2018). Experimental study of thermophoretic deposition of htgr graphite particles in a straight pipe. *Progress in Nuclear Energy*, **107**, 136–147. URL www.scopus.com. Cited By :4.

89. **Tratnig, A.** and **G. Brenn** (2010). Drop size spectra in sprays from pressure-swirl atomizers. *International Journal of Multiphase Flow*, **36**(5), 349–363.
90. **Weibel, E. R., A. F. Cournand,** and **D. W. Richards,** *Morphometry of the human lung*, volume 1. Springer, 1963.
91. **West, J. B.,** *Respiratory physiology: the essentials*. Lippincott Williams & Wilkins, 2012.
92. **Xi, J., T. Yang, K. Talaat, T. Wen, Y. Zhang, S. Klozik,** and **S. Peters** (2018). Visualization of local deposition of nebulized aerosols in a human upper respiratory tract model. *Journal of Visualization*, **21**(2), 225–237.
93. **Yeh, H.-C., O. Raabe, G. Schum,** and **R. Phalen** (1976). Tracheobronchial geometry: human, dog, rat, hamster. *Lovelace Foundation for Medical Education and Research, Albuquerque, NM*.
94. **Zhang, Z., C. Kleinstreuer,** and **C. Kim** (2000). Effects of asymmetric branch flow rates on aerosol deposition in bifurcating airways. *Journal of medical engineering & technology*, **24**(5), 192–202.

LIST OF PAPERS BASED ON THESIS

1. Mallik AK, Mukherjee S, Panchagnula MV. An experimental study of respiratory aerosol transport in phantom lung bronchioles. *Physics of Fluids*. 2020 Nov 1;32(11):111903.
2. Mallik, A.K., Sarma, T.P., Roy, A., Panchagnula, M.V. and Seshadri, S., 2020. PHASE DOPPLER PARTICLE ANALYSER (PDPA) CHARACTERIZATION AND MODELING OF SPRAYS FROM ORTHOGONALLY INTERACTING WATER AND AIR JETS. *Journal of Flow Visualization and Image Processing*, 27(2).